The Astrophysical Journal, 977:272 (26pp), 2024 December 20 https://doi.org/10.3847/1538-4357/ad90a5

A High-resolution Simulation of Protoplanetary Disk Turbulence Driven by the Vertical Shear Instability

Karim Shariff[1] and Orkan M. Umurhan[2]
[1] NASA Ames Research Center, Moffett Field, CA 94035, USA
[2] SETI Institute, Mountain View, CA 94043, USA
Received 2024 June 13; revised 2024 October 30; accepted 2024 November 3; published 2024 December 19

Abstract

A high-resolution fourth-order Padé scheme is used to simulate locally isothermal 3D disk turbulence driven by the vertical shear instability (VSI) using 268.4 M points. In the early nonlinear period of axisymmetric VSI, angular momentum transport by vertical jets creates correlated *N*-shaped radial profiles of perturbation vertical and azimuthal velocity. This implies dominance of positive perturbation vertical vorticity layers and a recently discovered angular momentum staircase with respect to radius (r). These features are present in 3D in a weaker form. The 3D flow consists of vertically and azimuthally coherent turbulent shear layers containing small vortices with all three vorticity components active. Previously observed large persistent vortices in the interior of the domain driven by the Rossby wave instability are absent. We speculate that this is due to a weaker angular momentum staircase in 3D in the present simulations compared to a previous simulation. The turbulent viscosity parameter $\alpha(r)$ increases linearly with r. At intermediate resolution, the value of $\alpha(r)$ at midradius is close to that of a previous simulation. The specific kinetic energy spectrum with respect to radial wavenumber has a power-law region with exponent -1.84, close to the value -2 expected for shear layers. The spectrum with respect to azimuthal wavenumber has a $-5/3$ region and lacks a -5 region reported in an earlier study. Finally, it is found that axisymmetric VSI has artifacts at late times, including a very strong angular momentum staircase, which in 3D is present weakly in the disk's upper layers.

Unified Astronomy Thesaurus concepts: Protoplanetary disks (1300); Hydrodynamical simulations (767); Hydrodynamics (1963); Accretion (14)

1. Introduction

1.1. General Introduction and Motivation

A question posed by astronomical observations of protoplanetary disks (PPDs), the history of our own solar system, and the results of theoretical and numerical modeling is: What types of flow, temperatures, and magnetic field configurations occur at different locations and during different periods of disk evolution, and how do they impact the dynamics and chemistry of solid particles which eventually form planets? The traditional motivation for studying flow turbulence in PPDs was to explain the so-called "anomalous viscosity" that gives rise to an accretion flow into the central star. More recently, however, the study of PPD turbulence is also very much motivated by the desire to explore its role in the pathway from micron-sized grains to asteroid-sized bodies, called planetesimals, that are believed to be the progenitors of rocky planets, the putative solid cores of gas giant planets, and whose remnants are today's asteroids, comets, and Kuiper Belt objects. This motivation is reflected in a wide ranging 19-author review (G. Lesur et al. 2022) examining various aspects of disk turbulence both in isolation and in interaction with particles and grains embedded in the gaseous nebula.

With respect to turbulence in isolation, it has come to be realized that the ionized fraction needed to sustain magnetorotational instability (MRI) occurs only at small radii near the star, large radii where the surface density is sufficiently low, and the upper layers of the disk (G. Lesur et al. 2022). At the same time, several hydrodynamic modes of instability have been identified. These are the subcritical baroclinic instability (SBI), convective overstability, zombie vortex instability, and vertical shear instability (VSI), the latter of which is the subject of the present work. Each of these is active for a certain range of radiative relaxation time, which depends on the number density and size distribution of dust grains.

VSI has received the lion's share of interest over the last few years since it is thought to be the most active turbulence generating mechanism within the solar nebula's midplane regions during the first million years (e.g., Y. Fukuhara et al. 2021), a time when the first planetesimals were made. Of the many open questions in this respect, perhaps the most pressing is the role that turbulence plays in bringing about or thwarting the formation of planetesimals (e.g., see recent discussions in U. Schäfer et al. 2020; P. Estrada & O. Umurhan 2023). In order to answer this, we must develop an understanding of the strength and structure of turbulence at different length scales in PPD settings. For example, how much of the turbulent energy generated by VSI at large scales propagates down to the scales where particles coalesce to form planetesimals? How does it subsequently influence particle dynamics at those scales? We take a much-needed step in this direction by examining VSI (without particles) at sufficiently high resolution to capture a larger range of its small-scale structure.

1.2. Physics of VSI and Previous Theoretical Work

The present work employs cylindrical coordinates (z, r, ϕ) which form a right-handed system with unit vectors satisfying

$\boldsymbol{e}_\phi = \boldsymbol{e}_z \times \boldsymbol{e}_r$, and $\boldsymbol{e}_\phi$ pointing *into* the page. The spherical radius is denoted $R = (z^2 + r^2)^{1/2}$.

Research on VSI in PPDs has its roots in work involving the radiative zones of differentially rotating stars (P. Goldreich & G. Schubert 1967; K. Fricke 1968). In that context, thermal diffusivity is much larger than kinematic viscosity, allowing displaced fluid elements to maintain their angular momentum but not their entropy. As explained by R. P. Nelson et al. (2013), the latter removes the stabilizing effect of vertical buoyancy, while the presence of a vertical shear allows the stabilizing effect of a positive radial gradient of angular momentum to be overcome for modes that have a sufficiently short radial wavelength.

V. Urpin & A. Brandenburg (1998) and V. Urpin (2003) were the first to suggest that VSI could be a source of turbulence in PPDs and present a local stability analysis, modeling radiative transfer using Fick's law for thermal conduction. The first simulations of VSI were performed by R. Arlt & V. Urpin (2004) using ZEUS-3D; they also present a simple local stability analysis for isothermal flow. Their simulations capture the correct growth rate of the instability and extend into the nonlinear regime, providing the first estimates of the turbulent α parameter arising from VSI. However, their nonlinearly saturated states seem inconclusive, particularly when comparing turbulent transport characteristics between their small and large radial domain simulations.

As such, the aforementioned work failed to generate interest until R. P. Nelson et al. (2013) accidentally encountered the instability while trying to test the basic state for an MRI simulation. They presented the first plots of the flow structure in axisymmetric simulations, as well as in a 3D simulation with an azimuthal domain size of $\Delta\phi = \pi/4$. These results demonstrate that well-developed VSI consists of radially narrow, vertically oriented structures of vertical velocity with alternating sign. They modeled radiative effects as a relaxation to the basic-state temperature and found that the flow is unstable only when the relaxation time, $t_{\rm rad}$, is comparable to or shorter than the orbital time. They also extended earlier local stability analyses into the vertically global regime.

R. P. Nelson et al. (2013) provided the impetus for many subsequent analytical and numerical investigations. M.-K. Lin & A. Youdin (2015) performed a detailed linearized analysis of the effect of radiative relaxation time and obtain the following local criterion for VSI to be active:

$$t_{\rm rad} \lesssim \frac{|r(\partial\Omega/\partial z)|}{N_z^2}. \tag{1}$$

Since the (stabilizing) Brunt–Väisälä frequency N_z increases more rapidly with $|z|$ than the vertical shear $\partial\Omega/\partial z$, surface modes in the upper regions of the disk are the first to be damped as $t_{\rm rad}$ increases. They obtain a key criterion for global instability:

$$\Omega_{\rm K} t_{\rm rad} < \frac{h|q|}{\gamma - 1}, \tag{2}$$

where $h \equiv H/r$ is the ratio of disk scale height to radius, q is the radial temperature exponent, and γ is the ratio of specific heats. Equation (2) says that VSI in thicker disks and those with a steeper radial temperature is less constrained by the relaxation time. Based on the assumption of a minimum-mass nebula model, M.-K. Lin & A. Youdin (2015) express the relaxation time in terms of an effective thermal opacity and find that VSI should be active in the intermediate region of the disk from $r = 5$ to 50 au. However, follow-up studies show that models with more massive disks or reduced depletion in the small grain population can sensitively alter the medium's opacity, leading to a larger range of the VSI active region (e.g., Y. Fukuhara et al. 2021; G. Lesur et al. 2022, Section 5.3).

In the limit where $\Omega_{\rm K} t_{\rm rad} \ll h|q|/(\gamma - 1)$, linear disturbances are isothermal. Several authors (R. P. Nelson et al. 2013; A. J. Barker & H. N. Latter 2015; O. M. Umurhan et al. 2016) have shown that the resulting system of linear perturbation equations may then be analytically examined in the radially local but vertically global limit, which extends previous fully local analyses (P. Goldreich & G. Schubert 1967; K. Fricke 1968; R. Arlt & V. Urpin 2004) and Boussinesq equation treatments (e.g., V. Urpin 2003). The main new feature contained in these semi-global treatments is that unstable modes are exponentially growing oscillations. O. M. Umurhan et al. (2016) show that the most unstable disturbances have a radial wavelength λ_r given by

$$\lambda_{r,\max} = \pi|q|h(r)H(r), \tag{3}$$

where $H(r)$ is the local disk scale height. Moreover, they show that modes become purely oscillatory (neither growing nor decaying) for disturbance wavelengths $\lambda_r > \lambda_{r,\rm marginal} = 2\lambda_{r,\max}$.

H. N. Latter & J. Papaloizou's (2018, henceforth L&P) theoretical study begins with a simple but informative setup, namely, incompressible uniform density flow in a local box that is uniformly sheared radially as well as vertically. This setup permits Fourier analysis with the wavevector dependent on time ($\boldsymbol{k} = \boldsymbol{k}(t)$), a trick due to Lord Kelvin (A. D. D. Craik et al. 1986) that eliminates terms which are linear in the coordinates. As is known (op. cit.), for such a setup the nonlinear term for each individual Fourier mode is zero, and therefore each Fourier mode is also a solution to the nonlinear equations. Thus, L&P note that a single mode can grow to arbitrary amplitude. In reality, a perturbation will consist of many modes, and therefore nonlinear interaction among them can lead to a saturated turbulent state. An elegant result (near their Equation (15)) is presented for the angle with respect to the vertical of the axisymmetric VSI jets. These jets are nearly vertical and their small tilt depends on the vertical shear. Another simple result is that the growth rate, σ, of the most unstable mode is proportional to the vertical shear:

$$\sigma \approx r|\partial\Omega/\partial z|, \tag{4}$$

for small vertical shear. Next, L&P go beyond the uniform density case to consider uniform stratification with the Boussinesq approximation and include temperature and momentum diffusivity. They find that radially short waves exploit thermal diffusion to circumvent buoyant stabilization. Finally, L&P consider secondary (or parasitic) instabilities generated by a primary one with velocity amplitude $V > 0$. The axisymmetric parasites take the form of Kelvin–Helmholtz (KH) modes generated on vertical jet shear layers of the primary VSI mode. A necessary condition for instability for moderate V is that the Rossby number

$$\mathrm{Ro}_V \equiv \frac{kV}{\Omega} \gtrsim 0.9262, \tag{5}$$

Table 1
Resolution Comparison between Representative Previous 3D Simulations (without Radiative Transport) and the Present One

References	p	q	h	$\Omega_K t_{\rm rad}$	$n_R \times n_\theta \times n_\phi$ or $n_r \times n_z \times n_\phi$	$n_R \times n_\theta \times n_\phi$ per H_0 or $n_r \times n_z \times n_\phi$ per H_0	ΔR or Δr	$R_0\Delta\theta$ or Δz	$\Delta\phi$
S. Richard et al. (2016)	−1.5	−2	0.20	0.05-0.5	500 × 200 × 300	250 × 20 × 38.2	$2H_0$	$10H_0$	$2\pi/4$
M. R. Stoll & W. Kley (2016)	−1.5	−1	0.05	0	1024 × 256 × 64	38 × 25.6 × 4.1	$27H_0$	$10H_0$	$2\pi/8$
M. R. Stoll et al. (2017)	−1.5	−1	0.05	0	600 × 128 × 1024	21 × 12.8 × 8.1	$29H_0$	$10H_0$	2π
N. Manger & H. Klahr (2018)	−2/3	−1	0.10	0	256 × 128 × 768	17.1† × 14.6 × 9.8	$15H_0$	$8.75H_0$	2π
N. Manger et al. (2020)	−1.5	−1	0.03	0	256 × 128 × 3402	19.2 × 18.3 × 16.2	$13.3H_0$	$7H_0$	2π
N. Manger et al. (2020)	−1.5	−1	0.10	0	256 × 128 × 1024	17.1 × 18.3 × 13.0	$15H_0$	$7H_0$	2π
Present	−1.5	−1	0.10	0	512 × 512 × 1024	74 × 74 × 16	$7H_0$	$7H_0$	2π

Note. H_0: scale height at the midradius of the computational domain. p: radial density exponent. q: radial temperature exponent. $h \equiv H_0/R_0$, the disk aspect ratio. R and r denote the radius in spherical and cylindrical coordinates, respectively. ΔR and Δr denote the width of the radial domain and include sponge regions. The resolution per scale height (H_0) is assessed at the midradius of the computational domain. †: the radial mesh for this simulation is logarithmic in R and the value 17.1 represents an average resolution per H_0.

where k is the wavenumber of the primary VSI mode. The presence of Ω in the denominator expresses the fact that rotation is stabilizing. If $\mathrm{Ro}_V \gg 1$ such that rotation does not play a role, then the characteristics of the secondary instability are like those of classical KH instability. For the nonaxisymmetric parasites, one must be mindful of the fact that the primary VSI mode also has *azimuthal* jets. In fact, if we make the approximation that $k_z \approx 0$, i.e., that the VSI mode has a negligible tilt relative to the vertical, then, Equations (11) and (15) in L&P imply that the amplitude of the azimuthal jets equals that of the vertical jets. The azimuthal jets are also susceptible to KH instability. However, the presence of background shear, rotation, and of both vertical and azimuthal vorticity modify its characteristics from classical KH instability; this will be seen in Section 4.3.

C. Cui & H. N. Latter (2022) continue the L&P analysis of parasitic modes and begin by noting that the primary VSI mode observed in global simulations is a standing wave in the vertical direction and radially propagating. They then look for a pair of inertial modes that grow by resonant interaction with the primary and find that there is an infinity of such pairs that can have much smaller radial wavelength than the primary mode. Numerical simulations will require many grid cells per primary wavelength $\lambda_{r,\max}$ to resolve them.

1.3. Previous Numerical Work

Table 1 lists parameters in some previous 3D simulations without radiative transport and compares them with the present one. The metric for numerical resolution given in the table, introduced by N. Manger & H. Klahr (2018), is the number of grid points per scale height H_0 at the midradius of the domain.

The computational study of S. Richard et al. (2016) was geared to the study of large vortices with vertical vorticity. They chose parameters to excite both VSI and SBI, which is known to generate such vortices. Indeed, their simulation produced elliptical vortices via the Rossby wave instability (RWI), which was studied by R. V. E. Lovelace et al. (1999) for razor-thin adiabatic disks. A necessary condition for the instability is that there be a local maximum of the quantity,

$$\mathcal{L} \equiv \frac{\Sigma}{2\omega_z}\left(\frac{P}{\Sigma^\gamma}\right)^{2/\gamma}, \tag{6}$$

where Σ is the surface density, ω_z the basic-state vertical vorticity, P the vertically integrated pressure, and γ the adiabatic exponent. The resulting vortex aspect ratio was found to depend on $t_{\rm rad}$. Table 1 shows that their radial resolution is superlative. Even though their radial domain width is only 2 scale heights, a sufficient number of structures is accommodated.

There is a series of 3D PLUTO simulations with radiative transport and stellar irradiation (M. R. Stoll & W. Kley 2014, 2016). The primary results are: (i) persistence of VSI with radiative transport, and (ii) a peak in the $T_{r\phi}$ Reynolds stress away from the midplane. M. R. Stoll et al. (2017) performed vertically isothermal simulations and studied the existence of a meridional mean flow due to Reynolds stress gradients, which we confirm in Section 4.9. Table 1 shows that these simulations are marginally resolved in the azimuthal direction, having ≈5 grid points per scale height along the circumference at midradius. M. Flock et al. (2020) also performed PLUTO simulations with radiative transport and stellar irradiation. Parameters were chosen to represent a typical T Tauri system. They employed a large number of grid points, $1024 \times 512 \times 2044$ ($n_R \times n_\theta \times n_\phi$), which gives 70 grid cells per scale height. Their main findings were that (i) VSI is able to vertically loft 1 mm grains such that their scale height ratio $H_{\rm grains}(r)/r = 0.037$; this is much larger than the value $H/r = 0.007$ for the HL Tau system, which is better fit by nonideal MHD simulations (M. Flock et al. 2017); and (ii) a large persistent vortex is formed by the RWI at a radial location near the inner radial boundary, where the thermal relaxation times becomes low enough that VSI becomes viable. This causes a peak in the turbulence $\alpha(r)$ parameter, which in turn leads to a dip in surface density and a maximum in the RWI indicator function $\mathcal{L}(r)$.

N. Manger & H. Klahr (2018) performed 3D simulations using PLUTO'S piecewise parabolic scheme. They observed multiple elliptic eddies in the midplane with anticyclonic vertical vorticity, lifetimes of hundreds of orbits, and aspect ratios >8. Such vortices are formed only for sufficiently large azimuthal domains with $\Delta\phi = \pi$ and $\Delta\phi = 2\pi$. Their specific kinetic energy spectrum with respect to the azimuthal wavenumber m has a steeper than $-5/3$ power-law region followed by a -5 power-law region. Our simulations obtain only the $-5/3$ range (Section 4.5).

N. Manger et al. (2020, henceforth M20) constitutes the latest 3D simulations prior to the present work. One of their cases has the same disk aspect ratio, and exponents of density and temperature as the present case, namely, $h = 0.1$, $p = -3/2$, and $q = -1$, respectively. Compared to their resolution per scale height in the radial and vertical directions, ours is about 4 times improved, while being comparable in the azimuthal direction. In addition, the Padé scheme we employ provides better resolution for the same number of grid points (S. K. Lele 1992). Another metric particularly suited to assess resolution in the meridional plane is the number of grid points per radial wavelength of the fastest-growing mode $\lambda_{r,\max}$ introduced in Equation (3). Most of the simulations listed in Table 1 have a temperature exponent of $q = -1$, for which case $h(r) = H_0/r_0$, and Equation (3) becomes

$$\lambda_{r,\max}(r) = \pi|q|\frac{H_0}{r_0}H(r). \tag{7}$$

Here, q is the radial temperature exponent such that $T(r) \propto (r/r_0)^q$, H_0 is the scale height at midradius (r_0), and $H(r)$ is the local scale height (see Section 2.1). To obtain the above-stated metric (at midradius), multiply the tabulated number of grid points per scale height in Table 1 by 0.31 for the $h \equiv H_0/r_0 = 0.10$ cases, and by ≈ 0.10 for the $h = 0.03$ case. Doing this implies that for $h = 0.10$, we have 22.9 points in the meridional plane per $\lambda_{r,\max}(r_0)$, while M20 have 5.7 points. For their $h = 0.03$ case, M20 have 1.9 points.

M20 varied the disk aspect ratio $h \equiv H_0/R_0$ and the density exponent p (see Equation (9)) and found that the eddy viscosity parameter $\alpha \propto h^{2.6}$. They also bolstered their 2018 findings concerning the specific energy spectrum and the formation of large persistent vortices (LPVs) in the midplane.

Most recently, J. D. Melon Fuksman et al. (2024a, 2024b, henceforth MF24a and MF24b, respectively) performed high-resolution axisymmetric simulations with two-moment radiative transport and frequency-dependent opacities. They find that as dust is depleted, VSI is excited only in the upper layers of the disk. They find that the specific angular momentum $j_\phi(r) = u_\phi r$ develops a staircase profile with respect to r, i.e., regions of flattened $j_\phi(r)$ separated by jumps. We confirm that this occurs in the axisymmetric case and weakly in the 3D case.

2. Setup, Basic State, and Simulation Parameters

2.1. Basic State

The initial condition for the present simulations consists of a basic state and perturbation. The basic state follows R. P. Nelson et al. (2013). The temperature, or equivalently the isothermal sound speed squared, varies as a power law with cylindrical radius

$$c_{\rm i}^2(r) = c_0^2(r/r_0)^q, \tag{8}$$

where r_0 is a reference radius. The temperature gradient is due to stellar heating. The midplane density is also assumed to follow a power law:

$$\rho_{\rm mid}(r) = \rho_0(r/r_0)^p. \tag{9}$$

The vertical scale height of the disk is

$$H(r) = c_{\rm i}(r)/\Omega_{\rm K}(r), \tag{10}$$

where the Keplerian angular velocity is

$$\Omega_{\rm K}(r) = \Omega_0(r/r_0)^{-3/2},\ \Omega_0 \equiv (GM/r_0^3)^{1/2}. \tag{11}$$

Substituting Equations (8) and (11) into Equation (10), we obtain

$$H(r) = H_0(r/r_0)^{(3+q)/2},\ H_0 \equiv c_0/\Omega_0. \tag{12}$$

We choose $q = -1$; for this case, $H(r)$ grows linearly with r. Therefore, $h(r) \equiv H(r)/r = H_0/r_0$.

Defining the spherical radius $R \equiv (r^2 + z^2)^{1/2}$, the density and azimuthal velocity profiles that satisfy vertical hydrostatic balance and radial centrifugal balance are given by R. P. Nelson et al. (2013) as

$$\rho(r, z) = \rho_0\left(\frac{r}{r_0}\right)^p \exp\left[\frac{GM}{c_{\rm i}^2}\left(\frac{1}{R} - \frac{1}{r}\right)\right], \tag{13}$$

$$u_\phi(r, z) = u_{\rm K}(r)\left[(p + q)\left(\frac{H}{r}\right)^2 + (1 + q) - \frac{qr}{R}\right]^{1/2}, \tag{14}$$

where $u_{\rm K}(r) = (GM/r)^{1/2}$ is the local Keplerian velocity.

In order to later compare values of the fluctuation vorticity relative to those in the basic state, Figure 1 plots the two nonzero components of the basic-state vorticity.

2.2. A Remark on the Basic State for VSI

The VSI basic state has an angular velocity that varies not only with cylindrical radius r but also with the vertical direction, z: $u_\phi = u_\phi(r, z)$. As the name implies, VSI is driven by the vertical gradient $\partial_z u_\phi$ of angular velocity. This gradient corresponds to the existence of a *radial* vorticity, ω_r,

$$\omega_r = \frac{1}{r}\frac{\partial u_z}{\partial \phi} - \frac{\partial u_\phi}{\partial z} = -\frac{\partial u_\phi}{\partial z}, \tag{15}$$

since $u_z = 0$ in the basic state. The presence of ω_r is attributed to a baroclinic torque that arises from the radial temperature gradient. However, since baroclinic torque produces *azimuthal* rather than radial vorticity, the effect is indirect, as we now explain. For the present case of infinitely rapid cooling, the equation of state is vertically isothermal:

$$p = \rho c_{\rm i}^2(r). \tag{16}$$

The rate of baroclinic vorticity production then becomes

$$\frac{1}{\rho^2}(\nabla\rho \times \nabla p) = \frac{1}{\rho}\frac{\partial c_{\rm i}^2}{\partial r}\frac{\partial \rho}{\partial z}\boldsymbol{e}_\phi. \tag{17}$$

Equation (17) says that the baroclinic term applied to the basic state produces *azimuthal* rather than radial vorticity. Considering the signs of the right-hand side (rhs), we conclude that $\omega_\phi > 0$ is produced in the upper disk, while $\omega_\phi < 0$ is produced in the lower disk. This vorticity induces a radial rather than azimuthal velocity.

To investigate the reason for the apparent conflict, consider the ϕ vorticity equation assuming axisymmetry; this is given as Equation (B11):

$$\frac{D}{Dt}\left(\frac{\omega_\phi}{\rho r}\right) = \frac{1}{\rho r^2}\frac{\partial u_\phi^2}{\partial z} + \frac{1}{\rho^2 r}\frac{\partial c_{\rm i}^2}{\partial r}\frac{\partial \rho}{\partial z}, \tag{18}$$

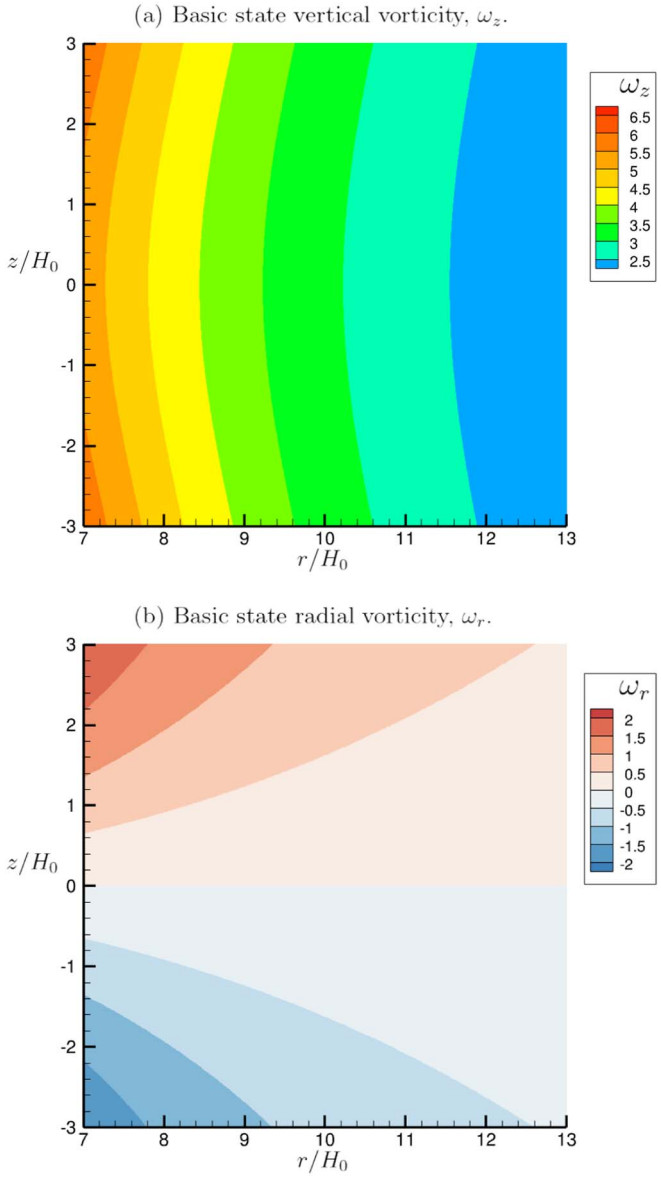

Figure 1. Basic-state vorticity.

where the second term is the baroclinic torque. If we assume both hydrostatic and centrifugal balance ($u_z = u_r = 0$), then $\omega_\phi = 0$ and we obtain

$$\frac{\partial u_\phi^2}{\partial z} = -\frac{r}{\rho}\frac{\partial c_i^2}{\partial r}\frac{\partial \rho}{\partial z}. \tag{19}$$

Equation (19) shows that vertical shear (=minus the radial vorticity) is proportional to the rate of baroclinic generation of azimuthal vorticity. However, it should be clear from the derivation that Equation (19) arises from the *constraint* of vertical and centrifugal balance. In an actual disk, this constraint will never be satisfied identically. Therefore, in the future it may be worthwhile to perform simulations starting with temperature and Keplerian gradients alone, and allow all other vorticity components to be freely generated. Presumably, the final stationary turbulent state will have the same statistics as with the conventional approach.

Table 2
Parameters for the Main 3D Run

Parameter	Value
No. of grid points, $n_r \times n_z \times n_\phi$	$512 \times 512 \times 1024$
Density exponent, p	$-3/2$
Temperature exponent, q	-1
Disk aspect ratio, H_0/r_0	0.10
Orbital period, T_0, at r_0	1
Density, ρ_0 at r_0	1
Sound speed c_0 at r_0	2π
Radial domain, $[r_{min}/H_0, r_{max}/H_0]$	[6.5, 13.5]
Vertical domain, $[z_{min}/H_0, z_{max}/H_0]$	$[-3.5, 3.5]$
Azimuthal domain	$\phi \in [0, 2\pi]$
Sponge width, δ_{sponge}/H_0	0.5
Decay period, t_{sponge}, for sponge	20 time steps
Number of processors	2048
CPU time per step	1.785 s
Intel processor	Haswell
Coeff. of artificial bulk viscosity, C_β	1.3
Strength of Padé filter, ϵ_{filter}:	
$t/T_0 \in [0, 300.27)$	0.125
$t/T_0 \in [300.27, 365.84)$	0.06
$t/T_0 \in [365.84, 372.33)$	0.03
$t/T_0 \in [372.33, 479.4]$	0.015
No. of time steps	862,584

For the basic state given by Equation (16), the vertical Brünt–Väisälä frequency squared $N_z^2 > 0$. This implies that buoyancy has a stabilizing effect when the flow is adiabatic. Buoyancy can be suppressed when the temperature of displaced parcels relaxes sufficiently rapidly to the basic state. In the present work, we assume that the radiative relaxation time is zero, i.e., that the vertically isothermal equation of state $p = \rho c_i^2(r)$ remains valid in the perturbed state.

2.3. Simulation Parameters

The simulation code PADÉ (K. Shariff 2024) uses fourth-order Padé differentiation (S. K. Lele 1992), which maintains accuracy for higher wavenumbers than conventional central finite-difference schemes of the same order. The simulations solve the hydrodynamic equations for compressible flow in cylindrical coordinates (r, z, ϕ) with a point-mass source of gravity at $r = z = 0$. The equation of state is locally isothermal:

$$p = \rho c_i^2(r), \tag{20}$$

where the isothermal sound speed $c_i(r)$ does not vary with time and has radial dependence given by Equation (8). This assumes rapid radiative relaxation of thermal fluctuations to the basic state.

Table 2 lists simulation parameters. The number of grid points is $512 \times 512 \times 1024$ ($n_r \times n_z \times n_\phi$). We choose r_0 to be the midradius of the computational domain. The density and temperature exponents are set to $p = -3/2$ and $q = -1$, respectively. The disk aspect ratio is chosen to be $h \equiv H_0/r_0 = 0.1$. These three parameters were chosen to be the same as for case `p1.5h0.1` in M20.

We are free to set three quantities to unity in the code: $H_0 = \rho_0 = T_0 = 1$, where T_0 is the Keplerian period at r_0. Therefore, the unit of velocity is H_0/T_0, i.e., scale heights per orbital period at r_0, and in code units the sound speed $c_0 = H_0\Omega_0 = 2\pi$.

The radial and vertical domains are both $7H_0$ long with a sponge strip of width $\delta_{\rm sponge}/H_0 = 0.5$ adjacent to each radial and vertical boundary. The flow field is relaxed to the basic state in the sponge regions with a characteristic relaxation time $t_{\rm sponge} = 20$ time steps. Zero normal velocity boundary conditions are applied at the radial and vertical boundaries. The azimuthal domain is a full circle with periodic boundary conditions. The number of grid points per H_0 is therefore $74 \times 74 \times 16$ in r, z, and ϕ (at r_0), respectively. The smaller resolution in ϕ is justified by the fact that Keplerian shear elongates vortical structures in this direction. However, a future check on this assumption should be made. To capture possible weak shocks in upper layers of the disk, artificial bulk viscosity, which acts on the dilatation $\nabla \cdot \boldsymbol{u}$, is activated with coefficient $C_\beta = 1.3$. However, we now believe this is unnecessary with a sponge layer at the upper and lower boundaries, and deactivated it in test simulations not reported here.

The initial condition is seeded with velocity perturbations of the form

$$\delta u = \epsilon_{\rm pert} M(z) \sum_{\boldsymbol{k}} {\rm Re}\{A(\boldsymbol{k}) e^{i\boldsymbol{k}\cdot\boldsymbol{x}}\} \tag{21}$$

for each component, where $A(\boldsymbol{k})$ is a complex number with unit amplitude and random phase, $\boldsymbol{k} \equiv (k_r, k_z, k_\phi)$, $\boldsymbol{x} \equiv (r, z, \phi)$, and $M(z)$ is a modulation. The radial wavenumbers, k_r, consist of a set of 11: a fundamental, seven harmonics, and three subharmonics. The fundamental has a wavelength of the most amplified mode:

$$\lambda_{r,\rm fund} = \pi |q| \frac{H_0}{r_0} H_0. \tag{22}$$

The wavenumbers k_z and k_ϕ both consist of a fundamental and 11 harmonics. The fundamental wavelengths in the z- and ϕ-directions equal the domain size in these directions, i.e., L_z and 2π, respectively. The amplitude was set to $\epsilon_{\rm pert} = 0.001 c_0$. Finally, a half-cosine modulation,

$$M(z) = \cos(\pi z/L_z),\ z \in [-L_z/2,\ L_z/2], \tag{23}$$

is applied to make perturbations vanish at the top and bottom boundaries.

2.4. Varying the Strength of the Padé Filter

The kinematic molecular viscosity in disks is so low that one cannot hope to perform a direct numerical simulation wherein all spatial scales down to molecular dissipation are resolved. Therefore, some treatment of unresolved scales is needed. For this, all simulations to date rely on the dissipation inherent in shock-capturing schemes to damp small-scale fluctuations. This is referred to as an "implicit" subgrid treatment (J. P. Boris et al. 1992; K. Ritos et al. 2018) to distinguish it from the use of an explicit subgrid model such as that of J. Smagorinsky (1963). Here, we adopt an implicit subgrid treatment using a Padé filter (S. K. Lele 1992) whose details and application procedure are summarized in Appendix A.

The Padé filter requires the setting of a parameter ($\epsilon_{\rm filter}$) which determines the strength of the filter. The main part of the run was for $t/T_0 \in [0,\ 300.27]$ during which the strength of the Padé filter was set to $\epsilon_{\rm filter} = 0.125$. This value was indicated as being conservative from test axisymmetric VSI runs presented in K. Shariff (2024). Figure 2 shows the components of the disturbance kinetic energy for the 3D run during this period.

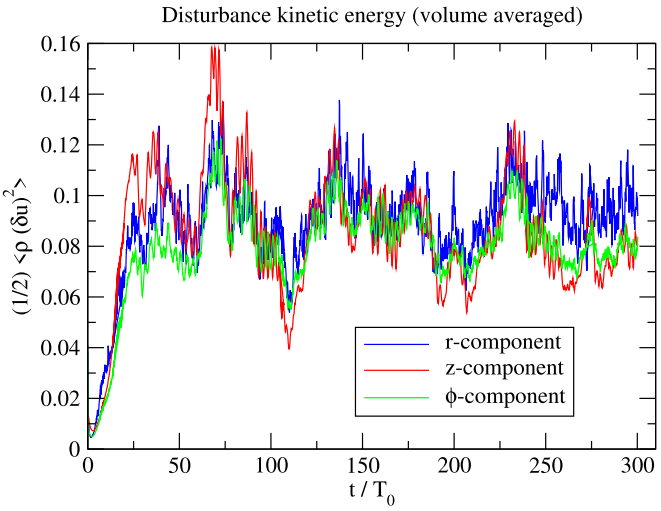

Figure 2. Time history of the components of the volume-averaged disturbance kinetic energy (relative to the basic state) for the 3D run in the period $t/T_0 \in [0,\ 300.27]$ during which the strength of the Padé filter was set to $\epsilon_{\rm filter} = 0.125$.

Time- and ϕ-averaged statistics of Reynolds stresses were taken for $t/T_0 \in [54.53,\ 300.10]$ during which the flow is statistically stationary. These stresses, together with the N. I. Shakura & R. A. Sunyaev (1973) $\alpha(r)$ they imply, will be shown in Section 4.7.

After the main part of the run was complete, we experimented with reducing $\epsilon_{\rm filter}$ to see if we could capture more fine-scale features and extend the power-law range in spectra without producing spurious 2Δ oscillations; energy spectra (Section 4.5) and inspections of the flow field confirmed that this was possible. The variation of $\epsilon_{\rm filter}$ with time is documented at the bottom of Table 2. The structure of the 3D flow field and associated energy spectra will be presented in the period when $\epsilon_{\rm filter} = 0.015$.

3. Axisymmetric Simulation: Early Nonlinear Stage

For all color contour plots in the paper, pure white pixels correspond to values that exceed the range of the color map.

The dynamics of axisymmetric VSI at early times are also present in the 3D case, although with less intensity and coherence. At later times, axisymmetric VSI contains strong artifacts (Section 5) that are not present in 3D. To enable a one-to-one comparison with the 3D case, the axisymmetric run was chosen to have the same parameters as the 3D run (with $\epsilon_{\rm filter} = 0.125$), except for a slight change in the number of grid points in order to evenly fit the 24 processors available on one node. The grid is 576^2 ($n_r \times n_z$).

3.1. Perturbation Velocity

The characteristic feature of axisymmetric VSI is the formation of counter-flowing vertical jets that remain coherent over the entire vertical extent of the disk; see Figure 3(a). It should be obvious that buoyancy suppression is needed for the maintenance of such jets. Upward jets are usually narrow and fast in the lower half of the disk and then widen and slow down as they travel into the upper half of the disk. Downward jets are narrow and fast for $z > 0$, then widen and slow down as they travel toward the lower half of the disk. This phenomenon may simply be due to the larger driving vertical shear for larger $|z|$.

As a result, a wider jet is located next to a narrow counter-flowing jet.

Figure 3(b) shows the azimuthal velocity perturbation, δu_ϕ. As mentioned earlier, the local linear stability analysis of L&P shows that δu_ϕ has the same magnitude as δu_z when tilt is neglected. The same is approximately true here.

Figure 3(c) shows that the product $\delta u_z \delta u_\phi$ is mostly $\gtrless 0$ for $z \gtrless 0$. This important fact is explained as follows. The specific angular momentum $j_z \equiv u_\phi r$ follows fluid elements for axisymmetric flow:[3]

$$\frac{Dj_z}{Dt} = 0. \tag{24}$$

Since the basic state j_z decreases away from the midplane, upward jets in $z > 0$ bring in higher j_z, leading to a positive product. Downward jets in $z > 0$ bring in lower j_z, also leading to a positive product. Similarly, upward jets in $z < 0$ bring in low j_z, leading to a negative product. Finally, downward jets in $z < 0$ bring in high j_ϕ, again leading to a negative product. Note that this explanation is linear because it involves the advection of the mean j_z by a perturbation u_z. This pattern of the $\delta u_z \delta u_\phi$ product will be reflected in the $T_{z\phi}$ Reynolds stress in 3D (Section 4.7).

Figure 4(a) was constructed to provide an alternate way of illustrating the fact, which a contour plot will soon make clear, that the perturbation ($\delta\omega_z$) of vertical vorticity,

$$\omega_z \equiv \frac{1}{r}\frac{\partial}{\partial r}(u_\phi r) = \frac{1}{r}\frac{\partial j_z}{\partial r}, \tag{25}$$

is dominated by thin positive layers. (Equation (25) is valid for axisymmetric flow only.) Figure 4(a) shows that the correlation between δu_ϕ (solid) and δu_z (dashed) is more remarkable than revealed in Figure 3. It also shows that both velocity components have N-shaped profiles such that regions of positive slope are much steeper than regions of negative slope. We note that in the lower half of the disk (not plotted), δu_z has mirrored N waves while δu_ϕ has normal N waves. The azimuthal vorticity is defined as

$$\omega_\phi \equiv \frac{\partial u_r}{\partial z} - \frac{\partial u_z}{\partial r}, \tag{26}$$

where the second term dominates in VSI. Therefore, for $z > 0$, an N profile for δu_z implies that $\delta\omega_\phi < 0$ shear layers dominate over $\delta\omega_\phi > 0$ shear layers. The opposite in true for $z < 0$.

N-shaped profiles for δu_ϕ (in both halves of the disk) implies that layers of positive $\delta\omega_z$ dominate. This feature is present in 3D but with lower intensity and regularity. The preference for $\delta\omega_z > 0$ is explained as follows. The basic-state $j_z(r)$ profile increases monotonically with r; see the dashed line in Figure 4(b). Consider the upper disk ($z > 0$) and an interface that separates a downward jet on the left and an upward jet on the right ($\downarrow\uparrow$). Recalling that the basic-state j_z is a maximum at the midplane, the downward jet on the left will lower j_z while the upward jet on the right will increase j_z. This will eventually lead to a positive jump in j_z with respect to r and an increase in positive ω_z since

$$\omega_z = \frac{1}{r}\frac{\partial}{\partial r}(u_\phi r) = \frac{1}{r}\frac{\partial j_z}{\partial r}. \tag{27}$$

Similarly, consider an interface that separates an upward jet on the left and a downward jet to its right ($\uparrow\downarrow$). This will reduce the slope of $j_z(r)$, leading to the flatter part of the j_z staircase and a lowering of $\delta\omega_z$. Each type of interface behaves in the opposite manner for $z < 0$. The continuation of a $\downarrow\uparrow u_z$ interface into the lower disk will now cause $j_z(r)$ to flatten and ω_z to decrease. Similarly, the continuation of a $\uparrow\downarrow u_z$ interface into the lower disk will cause $j_z(r)$ to steepen and ω_z to increase. This means that regions of $\omega_z > 0$ intensification in the upper disk will appear staggered relative to those in the lower half.

The staircase structure of $j_z(r)$ is shown as the solid line in Figure 4(b). In the 3D case (solid blue line), this pattern is less intense and coherent. H. Klahr et al. (2023), MF24a, and MF24b were the first to point out the formation of a $j_z(r)$ staircase for axisymmetric flow. The N waves in $u_\phi(r)$ simply reflect this staircase structure.

Figure 4(c) repeats Figure 4(a) at the midplane. While δu_z is comparable to its value at $z = 2H_0$, δu_ϕ is much weaker, and the correlation between δu_z and δu_ϕ observed at $z = 2H_0$ is absent. This is because the vertical gradient of j_z which drives the creation of δu_ϕ vanishes at $z = 0$.

3.2. Perturbation Vorticity

Figure 5 shows the perturbation vorticity field in the axisymmetric simulation. It attains values many times that of the basic-state vorticity with larger values as $|z|$ increases. From the range of the data, we conclude that the dominant component is azimuthal (Figure 5(a)). This will be reinforced below, where we present the probability density function (pdf) of each perturbation vorticity component. The azimuthal component is organized into shear layers that form the boundaries of the vertical jets.

In the upper disk, $\omega_\phi < 0$ (blue) shear layers are dominant. Such layers are adjacent to a thin sliver of opposite sign (red) vorticity, followed by a diffuse red region in between the shear layers. The opposite is true in the lower disk. These patterns can also be seen in Figure 9 (lower-right panel) of MF24a. The dominant sign pattern of ω_ϕ correlates with the N waves in $\delta u_z(r)$ discussed in Section 3.1. The shear layers display vortices created by the KH instability.

Figure 5(b) shows the perturbation, $\delta\omega_z$, of the vertical vorticity relative to the basic-state value. It is dominated by layers of $\delta\omega_z > 0$ consistent with the N waves in δu_ϕ and positive jumps in $j_\phi(r)$ as discussed previously (Section 3.1). These layers spatially coincide with the shear layers of azimuthal vorticity.

The radial perturbation vorticity (Figure 5(d)) is the weakest of the three components. Positive values are dominant in the upper disk, the opposite being true for $z < 0$.

Some of the above assertions are confirmed by the pdf of each vorticity component; see Figure 6, which uses semi-log axes. One observes that $\delta\omega_\phi$ (solid green curve) is indeed dominant. The inner part of its pdf is fit reasonably well by a Cauchy distribution (green dashed curve),

$$p(s) = \frac{c}{\pi(c^2 + s^2)}, \tag{28}$$

[3] For $p = \rho c_i^2(r)$, the baroclinic term does not enter the ω_z transport Equation (B13) for axisymmetric flow, and therefore the circulation $\Gamma_z = 2\pi j_z$ is unaffected by baroclinic torque.

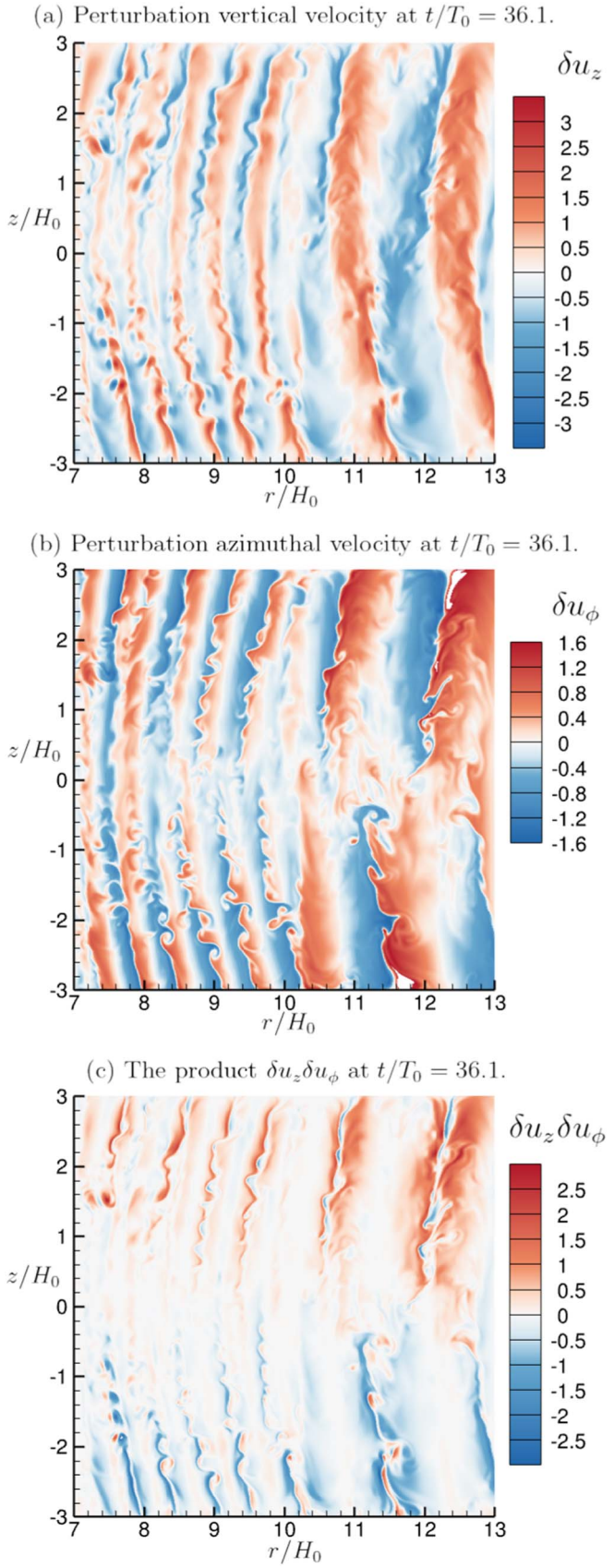

Figure 3. Perturbation velocity for the axisymmetric simulation on a 572^2 mesh at $t/T_0 = 36.1$. (a) Vertical velocity, u_z. (b) Perturbation azimuthal velocity, δu_ϕ. (c) The product, $\delta u_z \delta u_\phi$. Pure white regions represent values that are outside of the range of the color bar/legend.

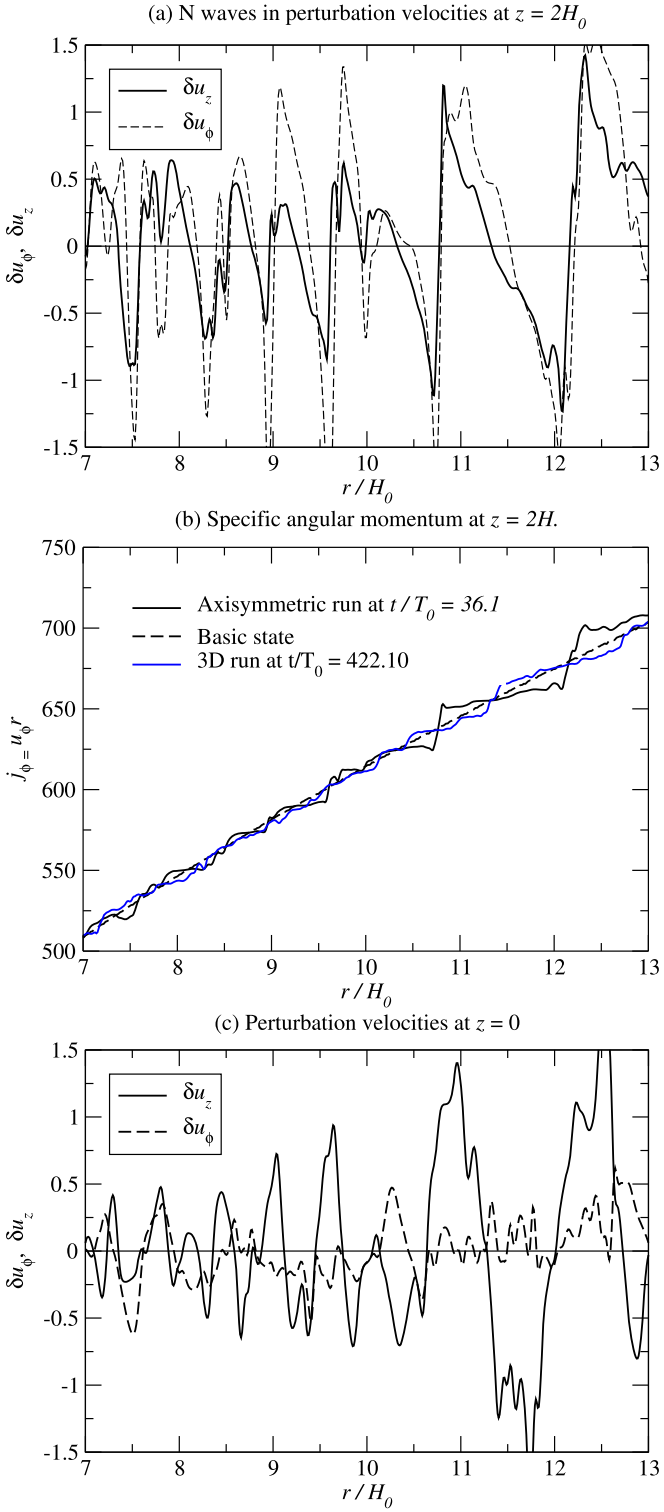

Figure 4. (a) Perturbation vertical and azimuthal velocities at $t/T_0 = 36.1$ showing their correlation and their N-waveform. (b) Specific angular momentum $j_z \equiv u_\phi r$ at $z = 2H_0$. Solid black line: at $t/T_0 = 36.1$ for the axisymmetric run. Solid blue line: at $t/T_0 = 422.10$ for the 3D run (azimuthal location $\phi = 0$). (c) Similar to panel (a) except evaluated at $z = 0$.

for $c = 4.35$. The choice of this distribution was inspired by J. Jiménez (1996), who obtains a similar result for the inner part of the velocity gradient pdf in 2D isotropic turbulence and for a collection of 2D Gaussian core vortices. For large vorticity

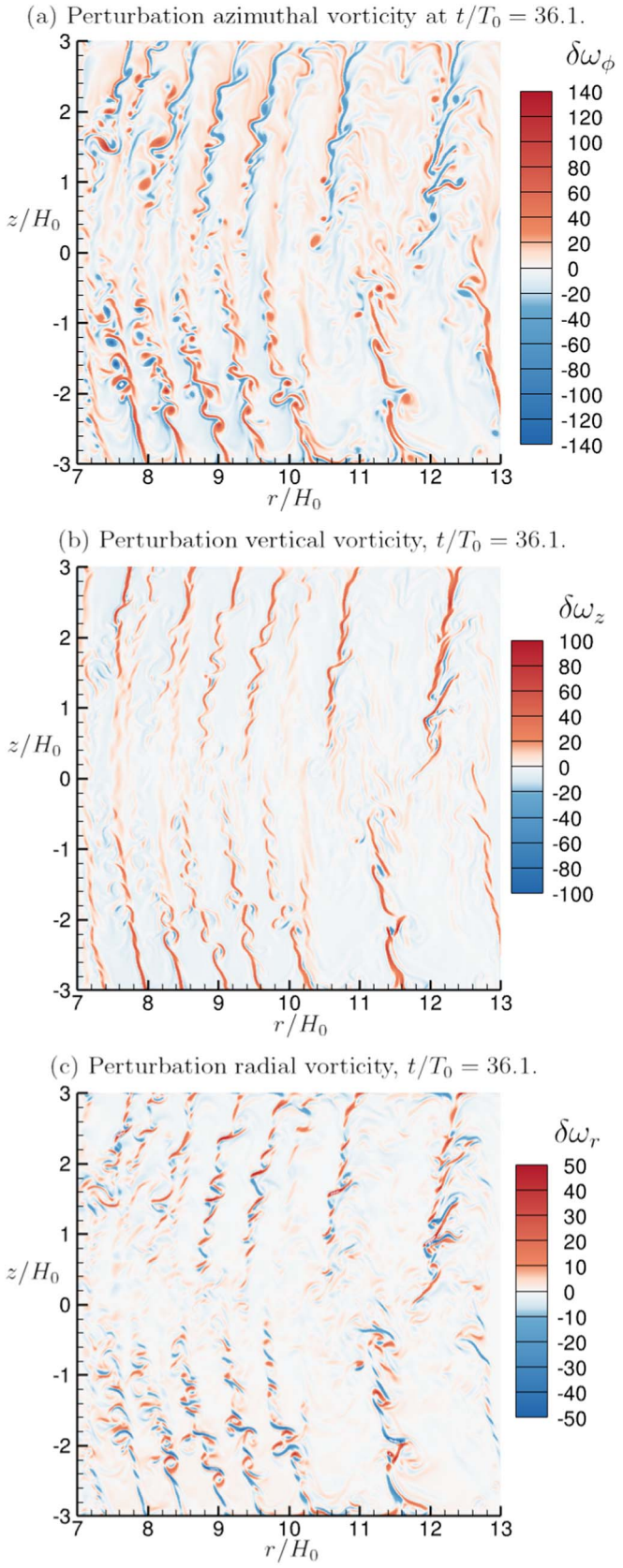

Figure 5. Perturbation vorticity for the axisymmetric run.

values in 2D isotropic turbulence, the analysis of G. Falkovich & V. Lebedev (2011) predicts exponential tails, which would show up as linear behavior on a semi-log plot. It is unclear

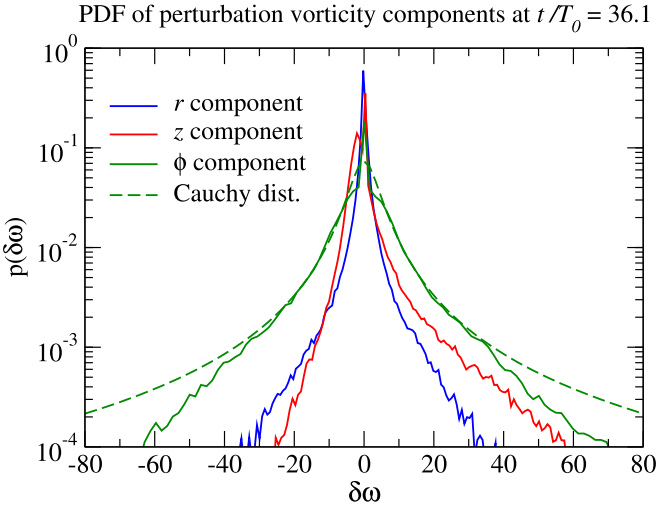

Figure 6. Probability density function of perturbation vorticity components for the axisymmetric run at $t/T_0 = 36.1$. The parameter c in the Cauchy distribution (Equation (28)) was set to $c = 4.35$ to obtain the green dashed curve.

whether this is true in the present case for $\delta\omega_\phi$. The red curve in Figure 6 confirms that $\delta\omega_z$ is skewed toward positive values consistent with Figure 5(b). To confirm the sign pattern for ω_ϕ, we plotted $p(\mathrm{sgn(z)}\delta\omega_\phi)$ (not shown to avoid clutter) and found it to be skewed toward negative values consistent with the color contour plot (Figure 5(a)).

3.3. Origin of the Sign Pattern of Azimuthal Vorticity

To understand the origin of the sign pattern of ω_ϕ, consider the two source terms, denoted T_1 and T_2, on the rhs of the ω_ϕ transport Equation (B11) multiplied through by ρr for convenience:

$$T_1 = \frac{1}{r}\frac{\partial u_\phi^2}{\partial z} \text{ and } T_2 = \frac{\partial c_i^2}{\partial r}\frac{\partial \log\rho}{\partial z}, \tag{29}$$

where T_1 is due to vertical shear and T_2 is the baroclinic term. The two terms balance in the basic state, i.e., $\breve{T}_1 + \breve{T}_2 = 0$, where a breve accent denotes a basic-state quantity. Therefore, it is more helpful to consider the deviations, δT_1 and δT_2, from the basic state.

Figure 7(a) shows that the vertical shear term δT_1 has the same overall sign pattern in shear layers as ω_ϕ. Its values lie in the range $\delta T_1 \in [-1200, 1200]$, which is much larger than the range $T_1 \in [-50, 50]$ in the basic state. On the other hand, Figure 7(b) shows that the baroclinic term δT_2 has a range $[-9.9, 8.5]$ that is much weaker than the basic state and does not show the same pattern. We therefore attribute the behavior of $\omega_\phi \approx \partial_r u_z$ to δT_1. Let us further ask: What determines δT_1? We have

$$\delta T_1 = \frac{1}{r}\frac{\partial}{\partial z}(\delta u_\phi^2) \approx \frac{2}{r}\breve{u}_\phi\frac{\partial}{\partial z}(\delta u_\phi) = \frac{2}{r^2}\breve{u}_\phi\frac{\partial}{\partial z}(\delta j_z). \tag{30}$$

Hence, the critical quantity is $\partial_z(\delta j_z)$, the perturbation in the vertical gradient of angular momentum, since the factor that multiplies it is >0 and known from the basic state. The quantity

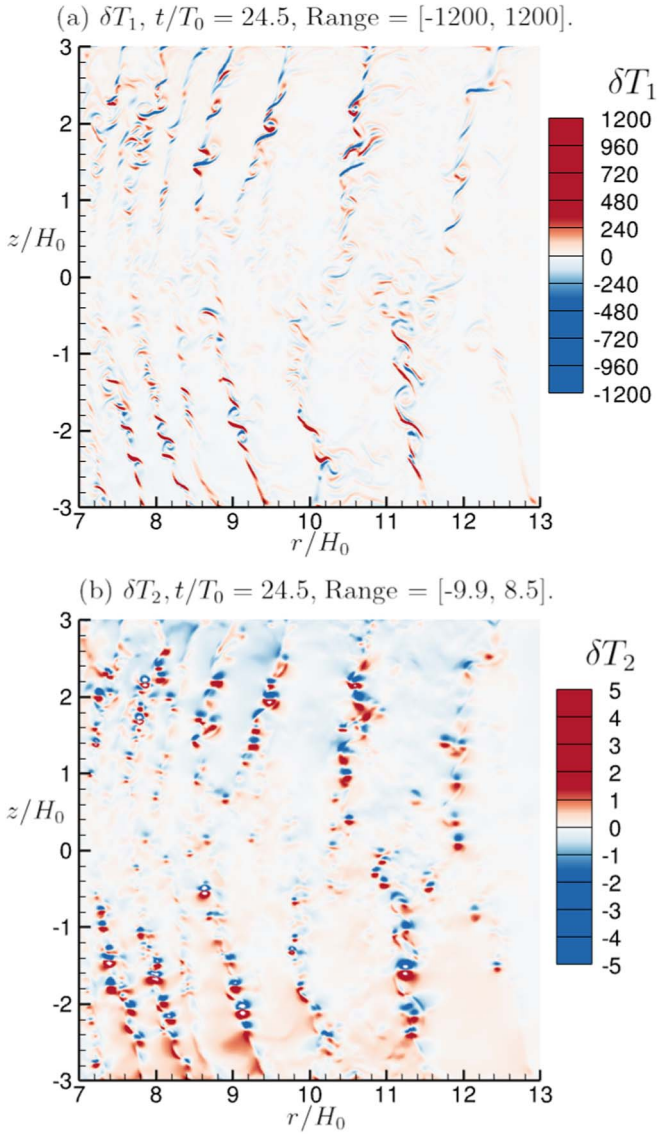

Figure 7. (a) Deviations from the basic state of the vertical shear term T_1 on the rhs of the transport Equation (B11) for azimuthal vorticity. (b) Similarly, the deviation T_2 (baroclinic term). In panel (b), values exceeding the range of the color legend are rendered in white. The actual range of values is indicated in the headings.

$\partial_z(\delta j_z)$ is obtained from the transport equation for j_z,

$$\frac{\partial j_z}{\partial t} + u_z \frac{\partial \breve{j}_z}{\partial z} \approx 0, \tag{31}$$

which is linearized about the basic state and assumes that vertical transport dominates radial transport. Differentiating Equation (31) with respect to z gives

$$\frac{1}{\delta t}\frac{\partial}{\partial z}(\delta j_z) = -\frac{\partial u_z}{\partial z}\frac{\partial \breve{j}_z}{\partial z} - u_z \frac{\partial^2 \breve{j}_z}{\partial z^2}. \tag{32}$$

We denote the two terms on the rhs of Equation (32) by T_3 and T_4.

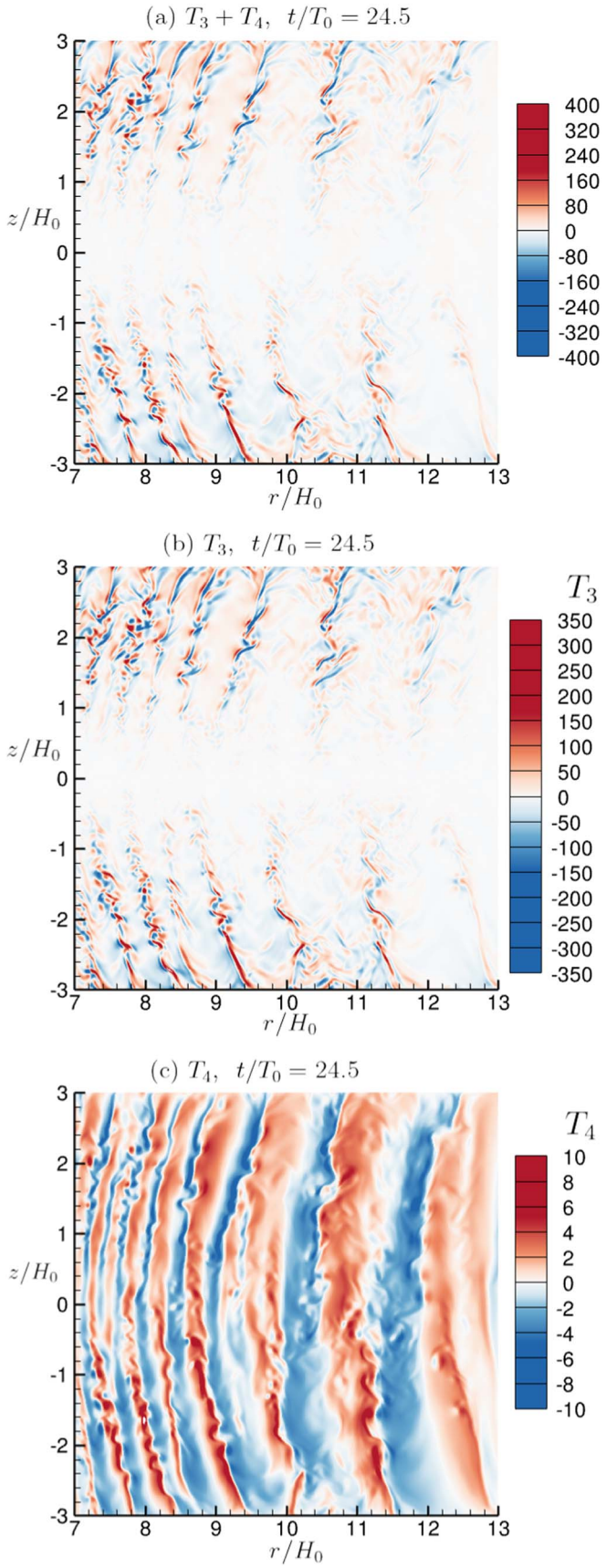

Figure 8. Terms in the transport Equation (32) for $\partial_z(\delta j_z)$.

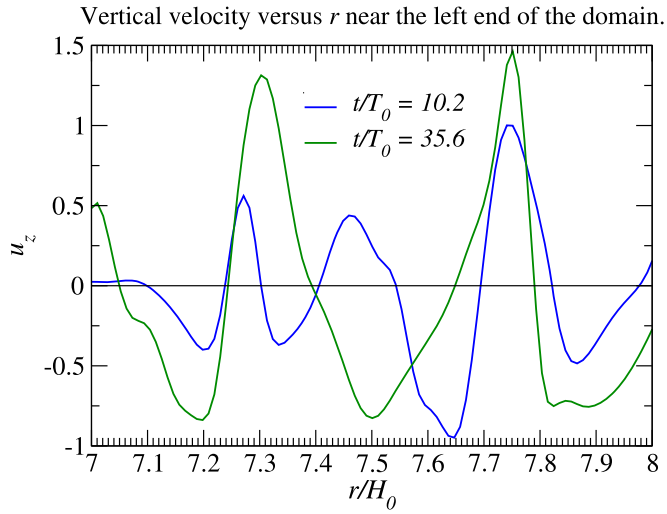

Figure 9. Profiles of $u_z(r)$ near the $r_{\min}$ boundary at $z/H_0 = -2$ for the axisymmetric run with a white-noise initial perturbation.

Figure 8 shows that $T_3 + T_4$ does indeed have the sign pattern of δT_1. By far, the greater contribution is from T_3. Finally, note that since $\omega_r = -\partial u_\phi/\partial z$, we can also write

$$\delta T_1 \approx -\frac{2}{r}\breve{u}_\phi \delta\omega_r. \tag{33}$$

If we refer back to Figure 5(c), we see that the sign pattern of $\delta\omega_r$ is indeed the opposite of δT_1.

3.4. Increase of Wavelength with Time

For the present case of $q = -1$ and $H_0/R_0 = 0.1$, Equation (7) for the most amplified linear instability wavelength becomes

$$\lambda_{r,\max} = \frac{\pi}{100} r, \tag{34}$$

which equals $0.24H_0$ at $r = 7.5H_0$, the midpoint of the interval to be plotted below. On the other hand, if we inspect Figure 5(b) we find that the radial wavelength is more than twice larger, being about $0.59H_0$ at the same radial location. To investigate this further, we ran the same case with a white-noise initial perturbation instead of a superposition of waves with random phases as described in Section 2.3. This change was made to eliminate any artifact that might be present due to the presence of subharmonics of $\lambda_{r,\max}$ in the wavy initial condition.

We find that wavelength increase is also observed with a white-noise perturbation. Figure 9 depicts profiles of $u_z(r)$ at two instants (for $z/H_0 = -2$) near the left end of the domain where the growth rate is the largest. An increase of wavelength with time is visually apparent. A value for the wavelength was obtained as the distance between downward zero crossings. At $t/T_0 = 10.2$ (blue curve), the average of the three wavelengths in the interval plotted is $\lambda_r = 0.24$, which equals the most linearly amplified wavelength at the midpoint of the interval. On the other hand, at $t/T_0 = 35.6$, the average of the two wavelengths is larger, namely, $\lambda_r = 0.37$. A temporal increase of wavelength can occur either due to nonlinearity or nonconstant coefficients in the linear phase, i.e., spatial variation of the basic-state gradient. Our guess is that the wavelength increase is due to nonlinearity and is related to a putative inverse cascade in axisymmetric VSI, discussed further in Section 5. Radial wavelength increase is also observed in the radiative hydrodynamic axisymmetric simulations of MF24b (their Figure 11).

T. Pfeil & H. Klahr (2021) performed an axisymmetric radiative hydrodynamics simulation using flux-limited diffusion and observed a sinusoidal vertical velocity at the midplane with amplitude increasing with radius; see their Figures 19 and 20. Their Figure 20 shows that the wavenumber $k_r H(r)$ decreases from 24 and 14 with increasing radius. On the other hand, the wavenumber from linear stability is

$$k_r H(r) = \frac{2}{|q|}\frac{R_0}{H_0} \approx 37, \tag{35}$$

since their $q = -1$ and $H_0/R_0 = 0.054$. Hence, their wavelengths are between a factor of 1.5 to 2.6 larger than for linear instability (for the locally isothermal equation of state). Curiously, their Figure 19 does not show any tendency for the wavelength to increase with time. This is at odds with the axisymmetric radiative hydrodynamic simulations of MF24b and should be investigated.

4. 3D Simulation

4.1. Perturbation Vorticity in a Meridional Plane

We now turn to the 3D simulation. Figure 10 shows components of the perturbation vorticity ($\delta\boldsymbol{\omega}$) in a meridional ($rz$) plane at $t/T_0 = 444.64$ during the period when the strength of the Padé filter has been reduced to $\epsilon_{\text{filter}} = 0.015$. As in the axisymmetric case, the strongest component is $\delta\omega_\phi$ (panel (b)) and consists of at least six turbulent shear layers (TSLs) that extend across the vertical extent of the disk; they are numbered from right to left and alternate in the dominant sign of $\delta\omega_\phi$. The predilection for negative layers for $z > 0$ and positive layers for $z < 0$ observed in the axisymmetric case (Figure 5(a)) is still noticeable. A more accurate description is that half of each TSL with predominantly $\delta\omega_\phi \lessgtr 0$ is more organized for $z \gtrless 0$, undergoes KH instability, and becomes disorganized or filamentary for $z \lessgtr 0$. This was also true in the axisymmetric case.

The vertical component ($\delta\omega_z$, Figure 10(c)) is the next strongest; however, its values are about one-third as large as in the axisymmetric case (compare with Figure 5(b)). Inspection of the vertical velocity (not shown) indicates that each TSL forms the boundary of a vertical jet. The numerical labels in panel (c) are placed at the same locations as in panel (b). One observes that $\delta\omega_z$ is dominated by positive values and exists on either the upper or lower half of each TSL. This makes $\delta\omega_z$ regions in the upper and lower halves staggered relative to each other. The explanation for this was given in Section 3.1. To the extent that the $\delta\omega_z$ TSLs remain coherent in the azimuthal direction (which is the case in the upper layers of the disk, as will be seen later), they correspond to a change in angular momentum as shown earlier (Figure 4, blue line). This is much weaker than in the axisymmetric case. We will see later that some of these layers undergo KH-type instability as predicted in the L&P analysis.

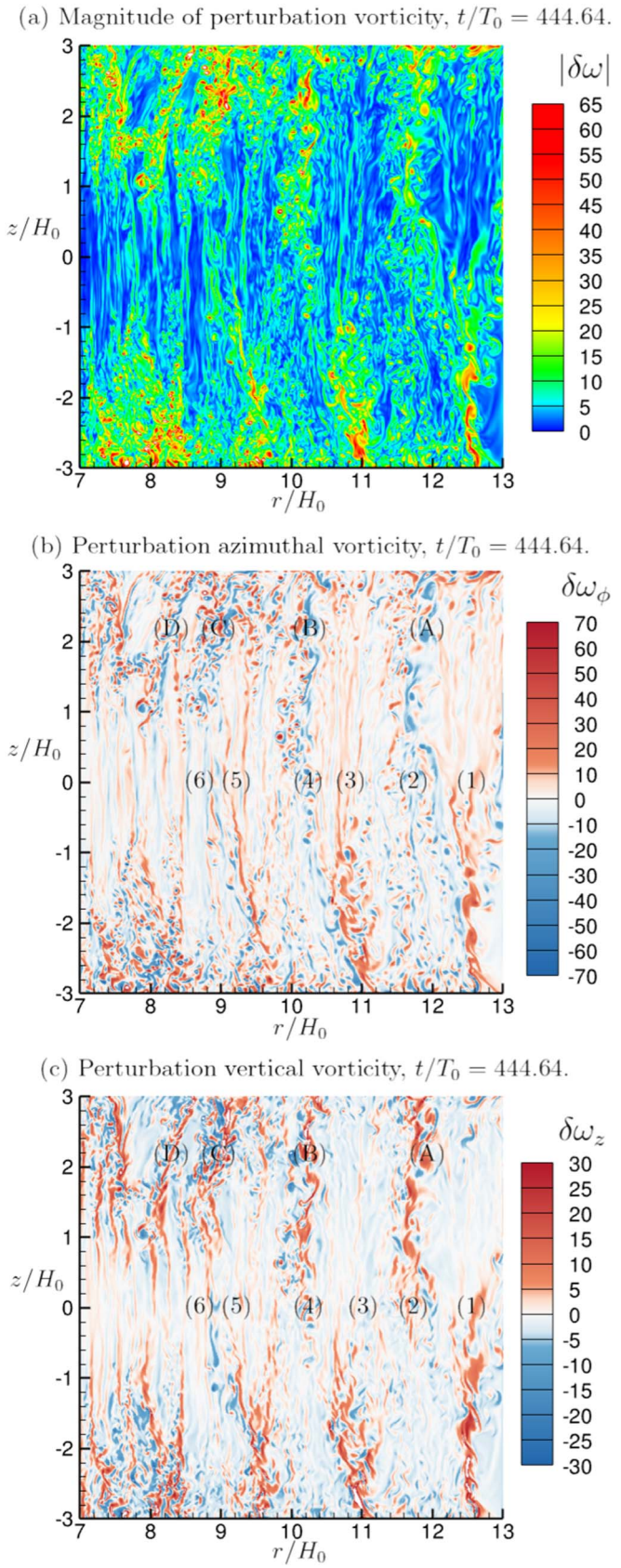

Figure 10. 3D run. Magnitude and components of the perturbation vorticity (relative to the basic state) in the $\phi = 0$ meridional plane at $t/T_0 = 444.64$. Turbulent shear layers are numbered (1)–(6) at the midplane and (A)–(B) at $z/H_0 = 2$.

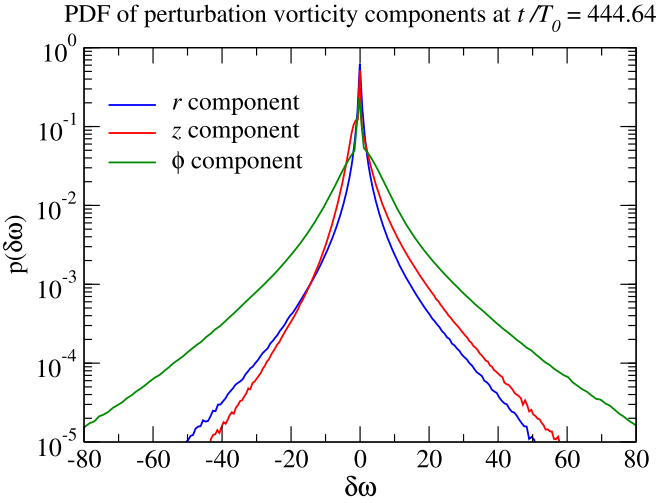

Figure 11. Perturbation vorticity pdf for the 3D run at $t/T_0 = 444.64$ sampled at 128 meridional planes.

One can define the Rossby number (Ro) as the ratio of $|\delta\boldsymbol{\omega}|$ to the local Keplerian vorticity; in code units, we have

$$\mathrm{Ro} \equiv \frac{|\delta\boldsymbol{\omega}|}{\pi(r/10)^{-3/2}}. \tag{36}$$

We find that $\mathrm{Ro} \approx 10$ in filaments that cross the midplane, and reaches values of 20 in KH eddies near the midplane. In the upper layers of the disk, Ro attains values as high as 125. A high value of Ro in a vortex or vortex layer indicates that it is minimally unaffected by Keplerian rotation and mean shear.

Figure 11 plots the pdf of perturbation vorticity components at $t/T_0 = 444.64$ sampled on 128 ϕ = constant planes. As in the axisymmetric case, $\delta\omega_\phi$ (green curve) is dominant. The preference for $\delta\omega_z > 0$ (red curve) is still present but to a smaller extent than in the axisymmetric case.

4.2. Midplane Vorticity

Since particles settle to the midplane, the turbulence there is of special interest. Figure 12 shows components of the perturbation vorticity relative to the basic state. The plot window is centered at $\phi = 0$ to allow comparison with the $\phi = 0$ meridional plane shown in Figure 10. The numerical labels are at the same positions as in Figure 10. The dotted lines indicate regions of width $\Delta r/H_0 = 1$ near the radial boundaries where the flow is affected by boundary conditions, as indicated later (Section 4.8) by anomalous local peaks in the turbulent $\alpha(r)$. The flow consists of bands where the flow is most nonaxisymmetric, i.e., not sheared along the azimuth. The bands correspond roughly to where the six TSLs observed in the meridional plane cross the midplane. Each band consists of lower-aspect-ratio $\delta\omega_z$ vortices of length $\lesssim 0.4H_0$. At outer radii, $\delta\omega_z$ vortices of both signs having similar aspect ratio are observed. However, at inner radii, $\delta\omega_z > 0$ is more filamentary because cyclonic $\delta\omega_z$ is easily sheared (S. Kida 1981) by the Keplerian mean (which is stronger at inner radii). Adjacent to each band is a region where perturbation vorticity is more sheared. One also observes that $\delta\vec{\omega}$ weakens with decreasing r; it is also more sheared, likely because the Keplerian shear increases as r decreases. It is emphasized that the $\delta\omega_z$ structures

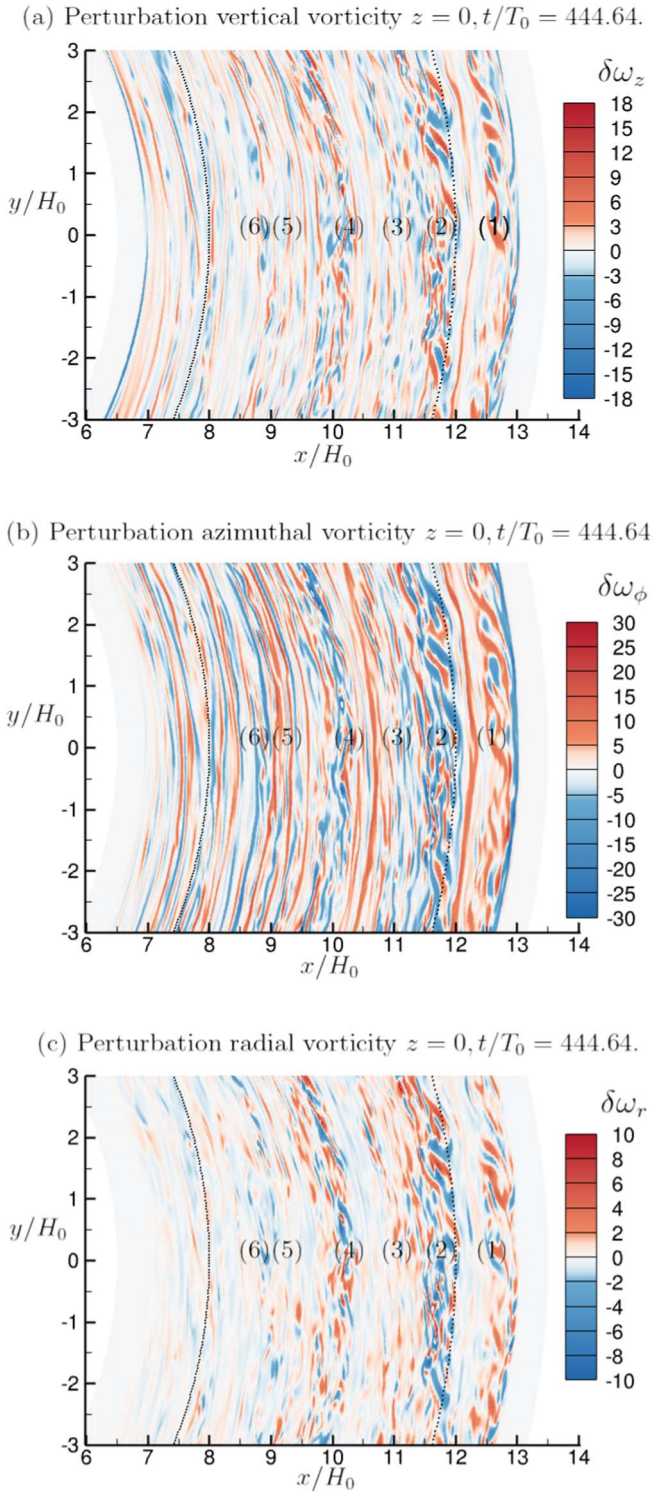

Figure 12. Components of the perturbation vorticity (relative to the basic state) in the midplane at $t/T_0 = 444.64$. The dotted lines indicate regions of width $\Delta r/H_0$ adjacent to each radial boundary that are affected by boundary conditions, as indicated later in the plot of the turbulent $\alpha(r)$ parameter.

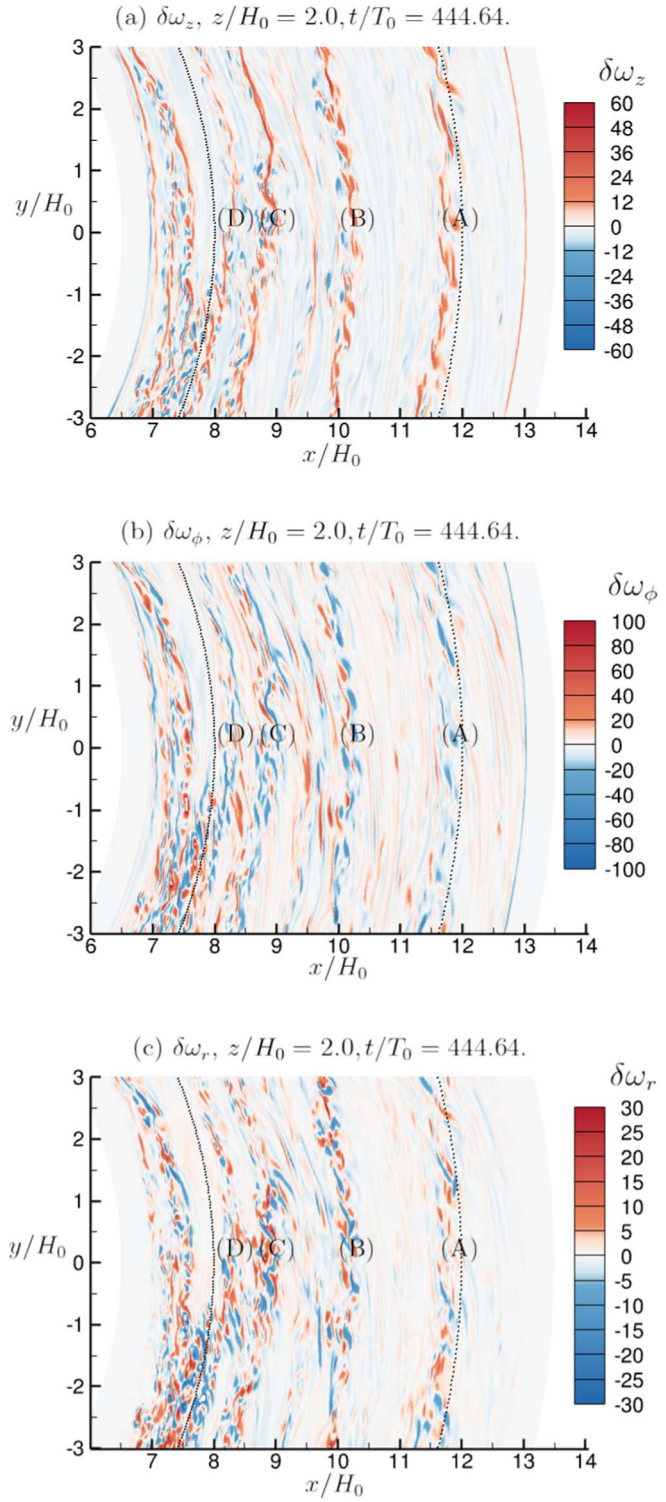

Figure 13. Components of the perturbation vorticity (relative to the basic state) at $z = 2H_0$ and $t/T_0 = 444.64$.

that have low aspect ratio (i.e., that are not elongated) are often associated with large values of $\delta\omega_\phi$ and $\delta\omega_r$.

The perturbation vorticity is dominated by the azimuthal component (Figure 12(b)), consistent with what is observed in a meridional plane and in pdfs (Figure 11). This component is associated with the jets of vertical velocity and is generally more sheared than $\delta\omega_z$. However, there are intermittent locations where ω_ϕ has smaller-aspect-ratio structures where, as mentioned above, other vorticity components are also active.

Figure 12(c) shows the perturbation radial vorticity. It has the lowest values among the three and is occasionally associated with other vorticity components. It most likely arises from the tilting and stretching of ω_z by ω_ϕ KH vortices.

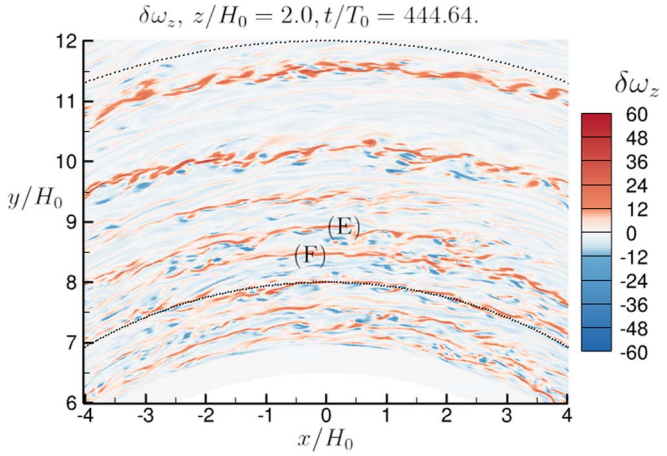

Figure 14. $\delta\omega_z$ at $z = 2H_0$ centered at $\phi = 90°$ ($t/T_0 = 444.64$).

An important difference in our simulations compared to M20 is the lack of LPVs. This difference will be discussed in Section 6.

4.3. Vorticity in a Horizontal Plane at Two Scale Heights

Perturbation vorticity components increase in magnitude away from the midplane and are therefore able to withstand the stabilizing effects of Keplerian rotation and shear.

Figure 13 shows components of $\delta\boldsymbol{\omega}$ at $z = 2H_0$. The letters (A)–(D) are placed at the same locations as in the meridional plane plots (Figure 10). Panel (a) depicts the vertical component; it is more than 3 times stronger than at the midplane. It is dominated by $\delta\omega_z > 0$ layers and displays KH-like instability for larger r, presumably because rotation and shear weaken as r increases. A few small elliptical $\delta\omega_z < 0$ structures are also present. Figure 13(b) shows that the $\delta\omega_z > 0$ layers are associated with negative ω_ϕ, just as in the axisymmetric case (Section 3.2). Recall from the axisymmetric case that the lower half of the disk has $\omega_\phi > 0$ in these layers. The values of ω_ϕ are about 3 times larger than at the midplane. Figure 13(c) shows that the weakest component, $\delta\omega_r$, is also about thrice as large as it is at the midplane.

4.4. Radial Wavelength in 3D

The $\delta\omega_z$ layers in Figure 13(a) (labeled (A)–(D)) can be used to infer a wavelength. These layers are coherent over a large azimuthal extent. We find that the ratio of the interlayer spacing ℓ_r to the local instability wavelength is 4.4 for layers (A) and (B), 4.5 for (B) and (C), and 2.4 for (C) and (D). Figure 14 shows $\delta\omega_z$ centered at $\phi = 90°$: the spacing ratio for layers (E) and (F) is 1.5. Therefore, the spacing ratio increases with radius. This means that the spacing $\ell_r(r)$ increases with r faster than $H(r)$ does. The inexorable radial wavelength growth with time present in axisymmetric VSI is halted in 3D and a time-invariant local radial length scale is established. An interesting question is whether $\ell_r(r)$ is an appropriate length scale for determining the turbulent viscosity ν_t.

4.5. Specific Kinetic Energy Spectra in the Midplane

Spectra of velocity squared (which we refer to as the specific kinetic energy) with respect to the radial and azimuthal

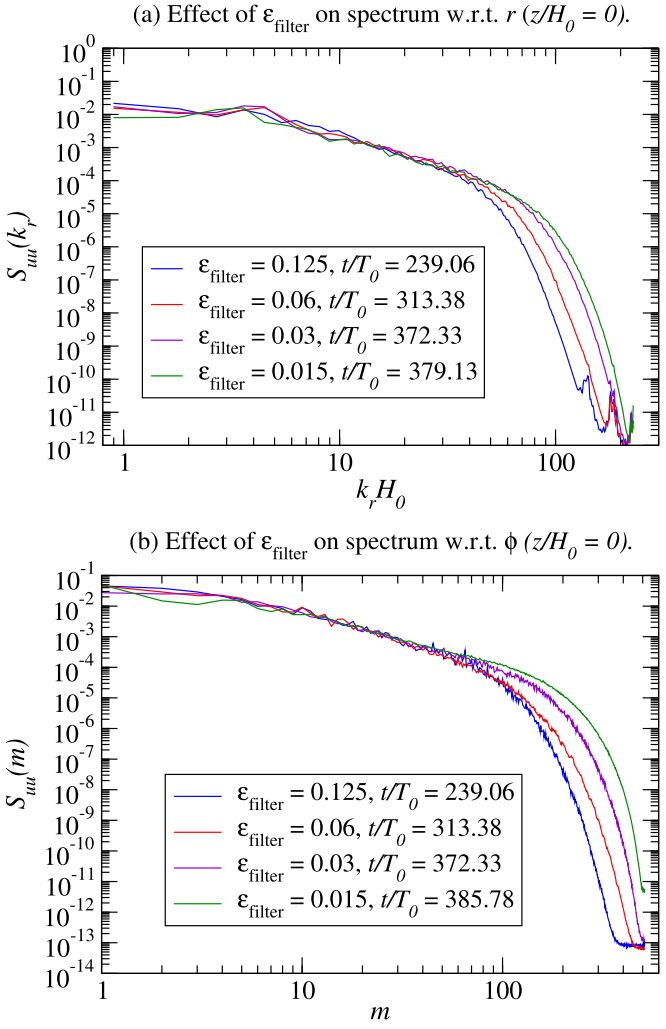

Figure 15. Effect of the strength of the Padé filter (ϵ_{filter}) on specific energy spectra in the midplane. (a) With respect to the radial wavenumber, k_r. (b) With respect to the azimuthal wavenumber, m. The units of S_{uu} are those of velocity squared, i.e., $(H_0/T_0)^2$.

directions are defined as

$$S_{uu}(k_r) = \hat{\boldsymbol{u}}(k_r) \cdot \hat{\boldsymbol{u}}^*(k_r), \tag{37}$$

$$S_{uu}(m) = \hat{\boldsymbol{u}}(m) \cdot \hat{\boldsymbol{u}}^*(m), \tag{38}$$

where the hat denotes a real to complex Fourier transform, a star denotes the complex conjugate, and m is the azimuthal wavenumber. To obtain $S_{uu}(k_r)$, a Hanning window was applied in r since it is not a periodic direction, after which an average was taken in ϕ. For $S_{uu}(m)$, an average was taken in r. Note that spatial inhomogeneity of the flow in r precludes a rigorous mathematical interpretation of these spectra.

Remark. Dr. J. David Melon Fuksman (2024, private communication) has suggested that since the flow has nonuniform density, it would be more appropriate to consider the quantity

$$E(\boldsymbol{k}) \equiv \mathrm{Re}\{\widehat{\rho\boldsymbol{u}}(\boldsymbol{k}) \cdot \hat{\boldsymbol{u}}^*(\boldsymbol{k})\}. \tag{39}$$

Note that since $\mathrm{Re}(fg^*) = \mathrm{Re}(f^*g)$ it does not matter whether we conjugate $\widehat{\rho\boldsymbol{u}}$ or $\hat{\boldsymbol{u}}$. J. Dutton (1963) has shown that the integral of Equation (39) with respect to $\boldsymbol{k}$ is proportional to the kinetic energy when the support of the velocity field $\boldsymbol{u}(\boldsymbol{x})$ is compact.

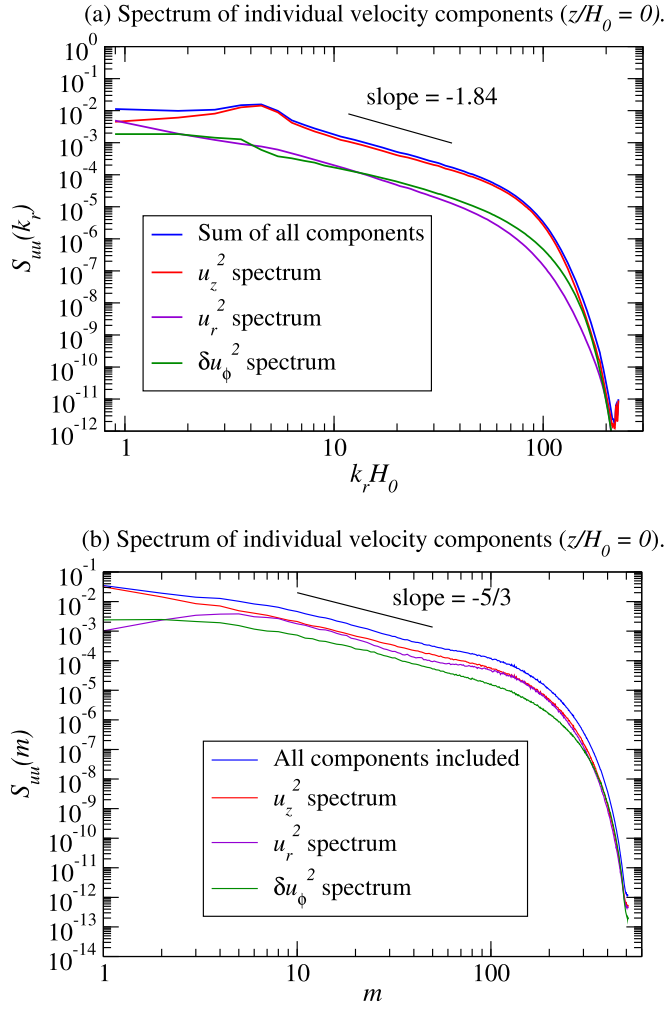

Figure 16. Specific energy spectra of individual velocity components in the midplane. Averaged over the time interval $t/T_0 \in [400.20, 452.55]$; $\epsilon_{\rm filter} = 0.015$. (a) With respect to the radial wavenumber, k_r. (b) With respect to the azimuthal wavenumber, m.

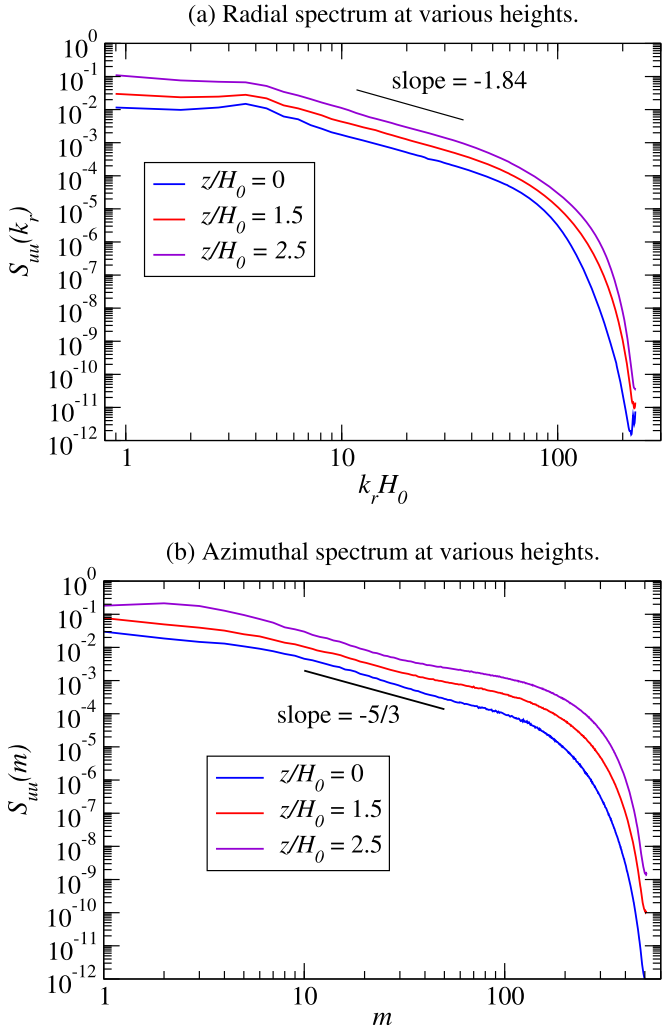

Figure 17. Specific energy spectra (all velocity components included) at different heights averaged over samples in the time interval $t/T_0 \in [444.6, 479.3]$ with spacing $\delta t/T_0 = 0.5$; strength of Padé filter $\epsilon_{\rm filter} = 0.015$. (a) With respect to the radial wavenumber, k_r. (b) With respect to the azimuthal wavenumber, m.

Figure 15 shows the effect of the filter strength $\epsilon_{\rm filter}$ on spectra. When $\epsilon_{\rm filter}$ is lowered, more of the power-law region (inertial range) is resolved without a significant upturn near the Nyquist wavenumber, which indicates that 2Δ oscillations are under control. This was confirmed by zooming in on vorticity contour plots: There are some isolated 2Δ oscillations, but they are not widespread.

Next, we investigate the anisotropy of the turbulence by plotting spectra of the different velocity components for the smallest filter strength ($\epsilon_{\rm filter} = 0.015$). To reduce statistical noise, spectra were computed for 50 fields in the period $t/T_0 \in [400.20, 452.55]$ and averaged.

Figure 16(a) displays the spectrum with respect to k_r and shows that u_z dominates the kinetic energy for most of the wavenumber range. A bump corresponding to energy injection by VSI is clearly observed at $k_r H_0 \approx 4.5$, which corresponds to a wavelength of $\ell_r \approx 1.4 H_0$. On the other hand, the most linearly unstable wavelength is $\lambda_{r,\rm max} = 0.31$ at the midradius of the domain. This bump is followed by a short (about 0.7 of a decade) power-law range with a slope of ≈ -1.84. This is close to the -2 slope that a jump in velocity across a shear layer would produce (A. A. Townsend & G. Taylor 1951).

Figure 16(b) displays spectra with respect to the azimuthal wavenumber m. The total energy (blue) has a slope close to the Kolmogorov value of $-5/3$. However, there is a small dip (relative to a straight line) at $m \approx 40$, which corresponds to a wavelength of $\approx 9°$; we see that the dip arises from the radial component (purple line). Again, u_z (red) is the dominant component, though not as strongly as was the case for k_r spectra. Radial velocity fluctuations (violet) are not much smaller than vertical velocity fluctuations (red) in the inertial (power-law) range. Azimuthal velocity fluctuations (green) have the least amplitude throughout the wavenumber range.

The azimuthal spectrum of N. Manger & H. Klahr (2018, their Figure 13) shows a broken power law consisting of a steeper than $-5/3$ slope followed by a slope of -5. On the other hand, we observe a a single power-law slope $\approx -5/3$ without a region of slope $= -5$. Also, whereas our spectra have a dissipation range in which the spectra fall off faster than any power law, the spectra of N. Manger & H. Klahr (2018) lack such a range. The reasons for these discrepancies remain to be investigated.

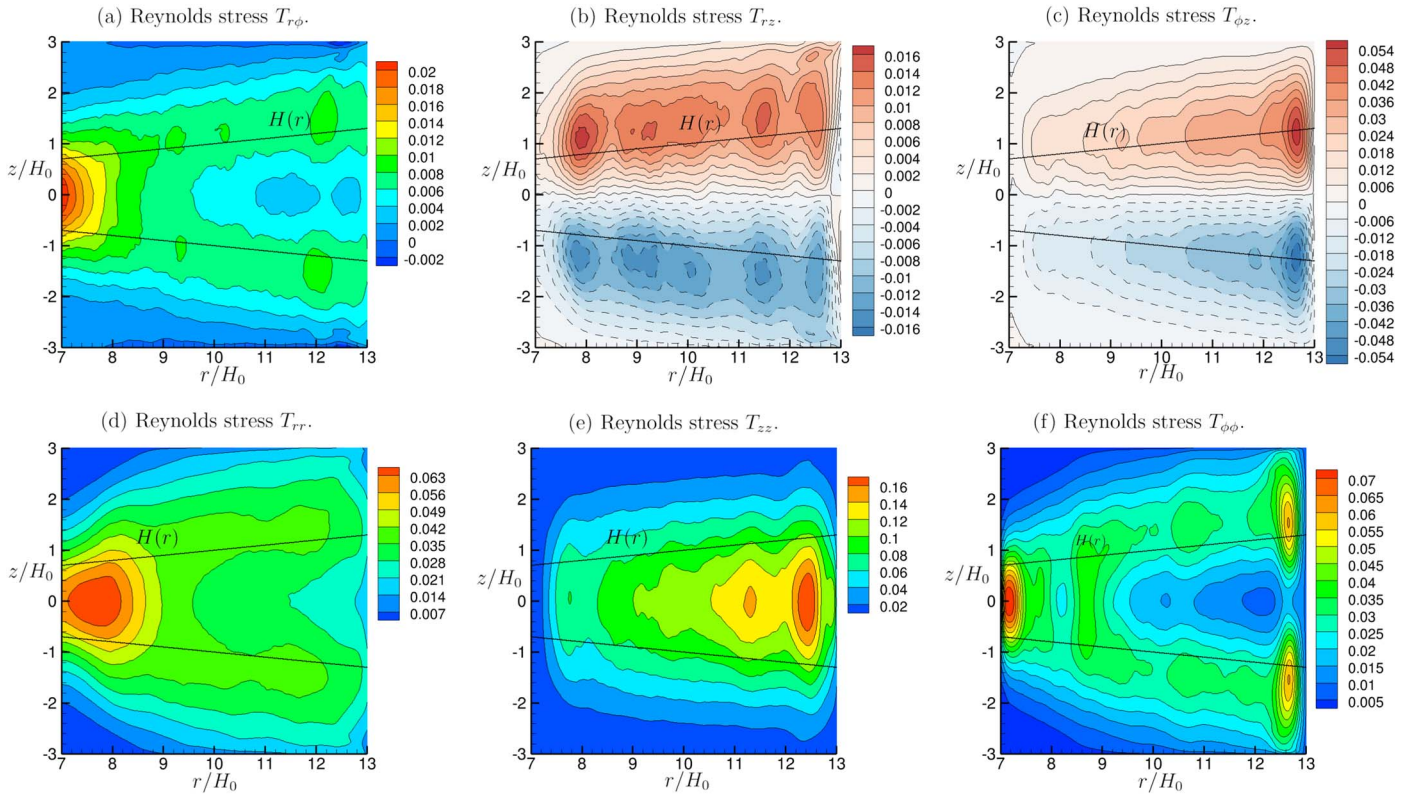

Figure 18. Reynolds stress tensor. Averaging was performed in the period $t/T_0 \in [54.53, 300.19]$. A region of $\Delta r/H_0 \approx 1$ at each radial boundary should be considered contaminated by boundary conditions.

4.6. Specific Kinetic Energy Spectra at Different Heights

Figure 17 shows radial and azimuthal spectra (with all velocity components included) at three different heights. The specific energy increases with height at each radial and azimuthal wavenumber. The radial spectrum has the same slope in the power-law region at all three heights. On the other hand, at higher $|z|$, the azimuthal spectrum displays a greater dip at about $m = 30$.

4.7. Reynolds Stresses

Here, we present maps of the Reynolds stress tensor, T_{ab}, in the meridional plane. The role of T_{ab} in the mean flow equations and the calculation of T_{ab} from simulation data is described in Appendices C and D, respectively. Time averaging was performed in the interval $t \in [54.53, 300.19]$ with samples spaced $\Delta t/T_0 \approx 0.5$ apart. Off-diagonal components of the Reynolds stress tensor are shown in the top row of Figure 18. Note that the component $T_{r\phi}$ enters the mean angular momentum Equation (C16). Away from the radial ends of the computational domain, where the flow is influenced by artificial numerical boundary conditions, $T_{r\phi}$ peaks away from the midplane at slightly above $z/H(r) \approx 1$. An off-midplane peak was also observed in M. R. Stoll & W. Kley (2014, their Figure 5). As will be seen in Section 4.9, this does not mean that the starward accretion mass flow peaks away from the midplane. The largest off-diagonal component is $T_{\phi z}$. To explain its sign pattern, positive and negative above and below the midplane, respectively, we invoke the mechanism given in Section 3.1 for the sign pattern of the product $\delta u_z \delta u_\phi$ in axisymmetric VSI, namely, the transport of a vertically varying mean specific angular momentum ($\partial_z \bar{j}_\phi \neq 0$) by vertical jets.

Figure 18 plots the normal components. One observes that the peak value of T_{zz} is about 3 times as large as that of T_{rr} and $T_{\phi\phi}$, reflecting the dominance of vertical jet-like fluctuations. In addition, T_{zz} peaks at the midplane. This is due to the presence of density (ρ) in the definition of the stresses, which rises faster toward the midplane than the vertical velocity rms decreases. On the other hand, T_{rr} and $T_{\phi\phi}$ peak above the midplane at $z \approx 1.5H_0$. This is consistent with the peak in $T_{r\phi}$ above the midplane. In fact, the correlation coefficient,

$$C_{r\phi} \equiv \frac{T_{r\phi}}{(T_{rr}T_{\phi\phi})^{1/2}}, \tag{40}$$

was found to be almost constant at ≈0.2–0.3 throughout the domain. This suggests that the shapes of the structures responsible for $T_{r\phi}$ are similar at all locations of the domain; only their intensity and/or size varies. The trace T_{kk} (not shown), which is twice the kinetic energy, peaks at the midplane but maintains high values up to $z \approx 1.5H_0$. Strong peaks in all the stresses near the left and right radial boundaries are considered to be artifacts due to boundary conditions.

4.8. The Turbulence α Parameter

The α parameter introduced by N. I. Shakura & R. A. Sunyaev (1973) is a nondimensional turbulent viscosity in vertically integrated accretion disk theory. Specifically,

$$\alpha(r) \equiv \frac{\nu_t(r)}{c_s(r)H(r)}, \tag{41}$$

where $\nu_t(r)$ is the turbulent viscosity. In our calculation, we took $c_s(r)$ and $H(r)$ to be the isothermal sound speed and scale

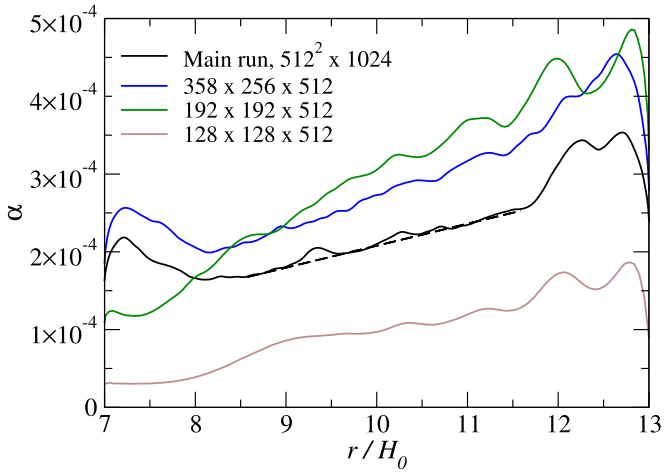

Figure 19. Shakura–Sunyaev turbulent viscosity parameter $\alpha(r)$ for runs with different resolutions. The straight dashed black line is $\alpha(r) = [2.0 + 0.28(r/H_0 - 10)] \times 10^{-4}$.

height of the basic state, respectively. In vertically integrated accretion disk analysis, which uses cylindrical coordinates, the vertically integrated turbulent torque appears as

$$\tau = \int_{-\infty}^{\infty} dz\, \frac{1}{r}\frac{\partial}{\partial r}(-r^2 T_{r\phi}). \tag{42}$$

The torque is then modeled using a turbulent viscosity as

$$\tau = \frac{1}{r}\frac{\partial}{\partial r}\left(r^2 \Sigma \nu_t r \frac{\partial \overline{\Omega}}{\partial r}\right), \tag{43}$$

where $\overline{\Omega}$ is the Reynolds-averaged vertically integrated angular rotation rate; the difference in $\alpha(r)$ was found to be very small when $\overline{\Omega}$ was replaced by the Keplerian value. Comparing Equations (42) and (43), one obtains

$$\nu_t = \frac{-\int_{-\infty}^{\infty} dz\, T_{r\phi}}{\Sigma r(\partial\overline{\Omega}/\partial r)}, \tag{44}$$

which when substituted into Equation (41) allows us to calculate $\alpha(r)$.

The solid black curve in Figure 19 shows $\alpha(r)$ for the most refined simulation. Away from the region affected by radial boundaries, we obtain linearly increasing behavior:

$$\alpha(r) = [2.0 + 0.28(r/H_0 - 10)] \times 10^{-4}. \tag{45}$$

An explanation one might initially suggest for the increase is the fact that the appropriate velocity scale for ν_t should be the driving vertical shear $\Delta u_\phi(r) = |u_\phi(r,\ z = H) - u_\phi(r,\ z = 0)|$ rather than the sound speed as assumed by N. I. Shakura & R. A. Sunyaev (1973). Unfortunately, however, $\Delta u_\phi(r) \propto c_i(r)$ for the VSI basic state. Another explanation one might suggest is that the radial wavelength $\ell_r(r)$ increases with r faster than $H(r)$ does (Section 4.4).

Figure 19 shows that with increasing resolution (starting with the brown curve) α initially rapidly increases to the green curve but then decreases to the blue and black curves. Inspection of the vorticity field for the brown case reveals minimal radial waviness of shear layers, which would contribute to a suppression of $T_{\phi r}$. Why should the highest-resolution case (black curve) have lower $\alpha(r)$ than the less resolved blue and green cases? We conjecture that large-scale waviness present at lower resolution breaks down into smaller

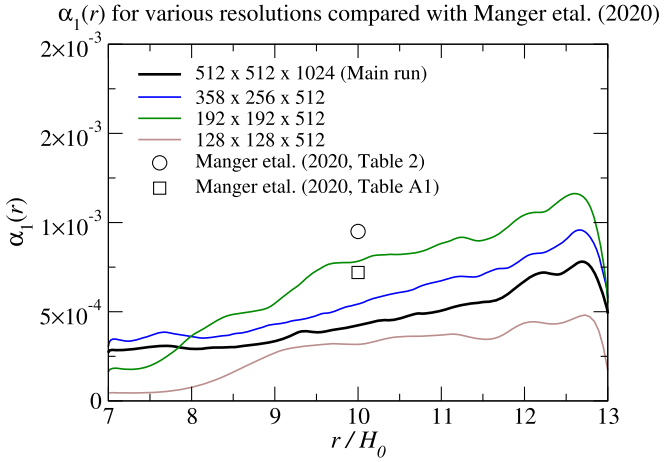

Figure 20. Turbulent viscosity parameter $\alpha_1(r)$ (in spherical coordinates) as defined by M20; see Equation (46). The lines are for the same cases as in Figure 19. ○: value from Table 2 of M20. □: value from Table A1 of M20.

vortices at higher resolution, leading to a smaller $T_{r\phi}$ correlation.

M20 use an alternate alpha parameter, defined as

$$\alpha_1(r) \equiv \frac{\int_{-\infty}^{\infty} dz\, T_{R\phi}}{c_i^2(r)\int_{-\infty}^{\infty} dz\, \overline{\rho}}, \tag{46}$$

where $T_{R\phi}$ is a stress in *spherical* coordinates and $\overline{\rho}$ is the mean density.[4] To calculate $\alpha_1(r)$ from our data in cylindrical coordinates, we use the fact that

$$T_{R\phi} = T_{r\phi}\sin\theta + T_{z\phi}\cos\theta, \tag{47}$$

where θ is the polar angle in spherical coordinates.

Figure 20 plots $\alpha_1(r)$ for the same cases as in Figure 19. Run p.1.5h0.1 of M20 has the same disk parameters as us. In their Table 2, they report a radially averaged value of $\alpha_1 = (9.5 \pm 2.1) \times 10^{-4}$, where the $\pm 2.1 \times 10^{-4}$ represents the amplitude of temporal fluctuations. This value corresponds to the period from 600 to 1000 orbits in their simulation. The temporal average $\alpha_1 = 9.5 \times 10^{-4}$ is shown as the ○ symbol in Figure 20. In their Table A1, they report a value of $\alpha_1 = (7.2 \pm 1.5) \times 10^{-4}$, which corresponds to the value in a putative stationary state at an earlier time of the simulation (H. Klahr 2024, private communication); this value also corresponds to the values plotted in their Figure 1 (bottom). Figure 20 shows that both of these values are close to our value at midradius for a lower resolution of $192 \times 192 \times 512$ grid points (green curve). Note that $\alpha_1(r) > \alpha(r)$ due to the additional contribution of the $T_{z\phi}$ stress component.

Finally, we mention in passing that H. H. Klahr & P. Bodenheimer (2003), M. R. Stoll & W. Kley (2016), and M20 calculate $T_{R\phi}$ using (their Equations (23), (6), and (4), respectively)

$$T_{R\phi} = \overline{\rho u_R u_\phi} - \overline{\rho u_R}\ \overline{u_\phi}, \tag{48}$$

[4] We had not noticed this until Dr. J. David Melon Fuksman pointed it out to us.

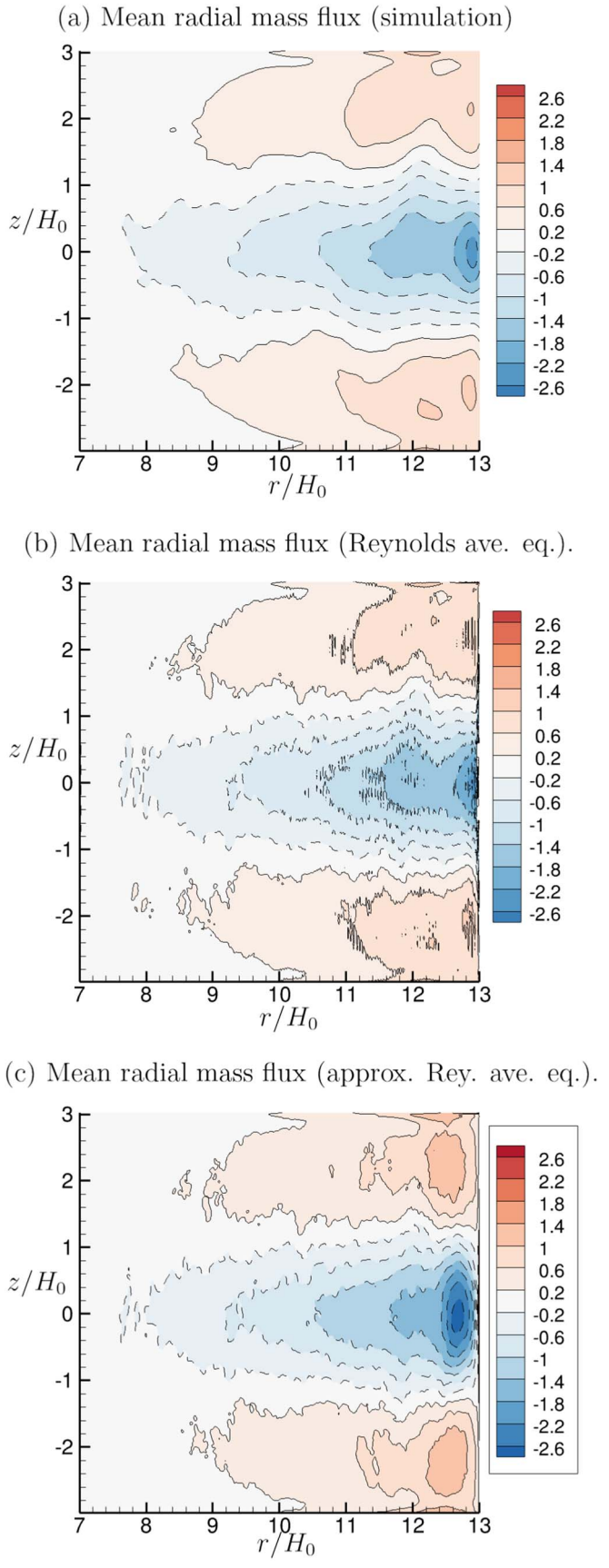

Figure 21. Mean radial mass flux $\dot{m} = 2\pi r\overline{\rho u_r}$. (a) Simulation. (b) From Equation (50), a consequence of the Reynolds-averaged angular momentum equation. (c) From Equation (50), after assuming that the Favre-averaged velocity $\tilde{u}_\phi$ is Keplerian.

which does not obey the symmetry property of the Reynolds stress. On the other hand, Equation (D8) gives

$$T_{r\phi} = \overline{\rho u_r u_\phi} - \frac{\overline{\rho u_r}\ \overline{\rho u_\phi}}{\overline{\rho}}, \tag{49}$$

which is symmetric. When density fluctuations are small, which is true in the present case, the error in Equation (48) is small.

4.9. Mean Radial Mass Flux

Figure 21(a) shows the mean radial mass flux (per unit height),

$$\dot{m} \equiv 2\pi r\overline{\rho u_r}, \tag{50}$$

obtained from the simulation. This flux is starward (<0) for approximately $|z| < H_0$ and radially outward otherwise. Such a mean radial flow was first identified by M. R. Stoll et al. (2017, their Figure 1).

This flux arises from turbulent stress gradients and can be derived from the Reynolds-averaged angular momentum Equation (C16). For stationary turbulence in which statistics do not depend on time, this equation becomes

$$\frac{\partial}{\partial r}[r^2(\bar{\rho}\tilde{u}_\phi\tilde{u}_r + T_{\phi r})] + r^2\frac{\partial}{\partial z}(\bar{\rho}\tilde{u}_\phi\tilde{u}_z + T_{\phi z}) = 0. \tag{51}$$

Taking the derivative with respect to r, using the Reynolds-averaged mass conservation equation,

$$\frac{1}{r}\frac{\partial}{\partial r}(r\bar{\rho}\,\tilde{u}_r) + \frac{\partial}{\partial z}(\bar{\rho}\,\tilde{u}_z) = 0, \tag{52}$$

solving for $\tilde{u}_r$, and using the definition in Equation (50), one obtains

$$\dot{m} = \frac{2\pi}{\partial_r(\tilde{u}_\phi r)}\left[-\frac{\partial}{\partial r}(r^2T_{\phi r}) - \frac{\partial}{\partial z}(r^2T_{\phi z}) - r^2\bar{\rho}\,\tilde{u}_z\frac{\partial\tilde{u}_\phi}{\partial z}\right]. \tag{53}$$

Figure 21(b) shows that the mass flux given by Equation (53) agrees with the simulation (as it should) apart from statistical error. This gives us confidence in the computation of the stress tensor. If one introduces the assumption that $\tilde{u}_\phi$ varies weakly with z, then the last term in Equation (53) disappears. If one further assumes that it is nearly Keplerian, i.e., $\tilde{u}_\phi \approx u_K = (GM/r)^{1/2}$, then we get

$$\dot{m} \approx \frac{4\pi}{u_K}\left[-\frac{\partial}{\partial r}(r^2T_{\phi r}) - \frac{\partial}{\partial z}(r^2T_{\phi z})\right]. \tag{54}$$

Equation (54) is analogous to Equation (7) in M. R. Stoll et al. (2017). Figure 21(c) shows that the result of Equation (54) agrees well with the exact result, except near the right end of the domain where it overpredicts the mass flux.

Note that because $T_{\phi z}(z)$ is antisymmetric about $z = 0$, the second term in Equation (54) is nonzero even at the midplane. Therefore, gradients of both $T_{\phi r}$ and $T_{\phi z}$ determine the accretion flow even at the midplane. If one integrates Equation (54) with respect to z one gets the result that the net mass flow rate depends only on $T_{\phi r}$, which is consistent with vertically integrated accretion disk theory.

The present result implies that turbulence can lead to secondary meridional flows that can be more complex than merely a starward accretion flow. This fact is important for the

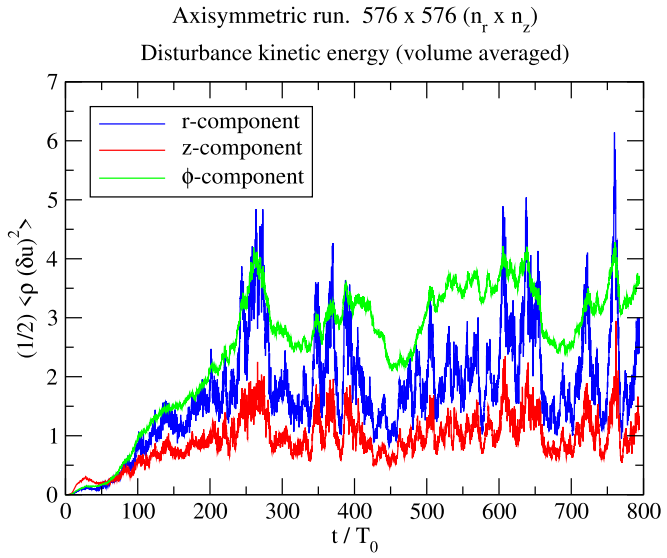

Figure 22. Time history of the volume-averaged perturbation kinetic energy for the axisymmetric run.

transport of solids in disks; however, we emphasize, as have M. R. Stoll et al. (2017), that solids can be transported by turbulent diffusion alone without the presence of a mean flow.

5. Late-time Artifacts in the Axisymmetric Simulation

Two artifacts arise at late times when the flow is constrained to be axisymmetric. These are (i) the specific angular momentum, $j_z = u_\phi r$, develops a high-amplitude and vertically coherent staircase structure, first observed by H. Klahr et al. (2023), MF24a, and MF24b; this is present only very weakly in the 3D case (Figure 4(b), blue curve) in the upper layers; and (ii) vortical structures merge into larger structures, and the flow resembles the inverse cascade of 2D turbulence. We now discuss these features.

Figure 22 shows the domain-averaged fluctuation kinetic energy components relative to the basic state. Compared to the 3D run (Figure 2), a statistically stationary state is reached very much later (at about $t/T_0 \approx 300$). This observation is not without precedent. The high-resolution axisymmetric VSI simulation (`dg3c4_1024`) of MF24a (their Figure 12, red curve) does not reach a stationary state even after about 1300 orbits when the simulation stops. It should also be noted that this case has a false and temporary stationary state up to about 600 orbits, after which the energy begins to rise again. Their lower-resolution case (`dg3c4_512`) exhibits a false period of stationarity up to 3000 orbits, after which the kinetic energy begins to rise again. The axisymmetric runs of L. Flores-Rivera et al. (2020) reach a stationary state after 100 orbits and were run to a final time of 200 orbits. Given the potential for false and temporary periods of stationarity in axisymmetric runs, caution must be exercised before concluding that a true stationary state has been reached.

Given that flow length scales increase with time in our simulation (see below) as well as in the simulations of M24a, i.e., that there is an inverse cascade, the time to reach stationarity in any given simulation would depend on the radial domain size.

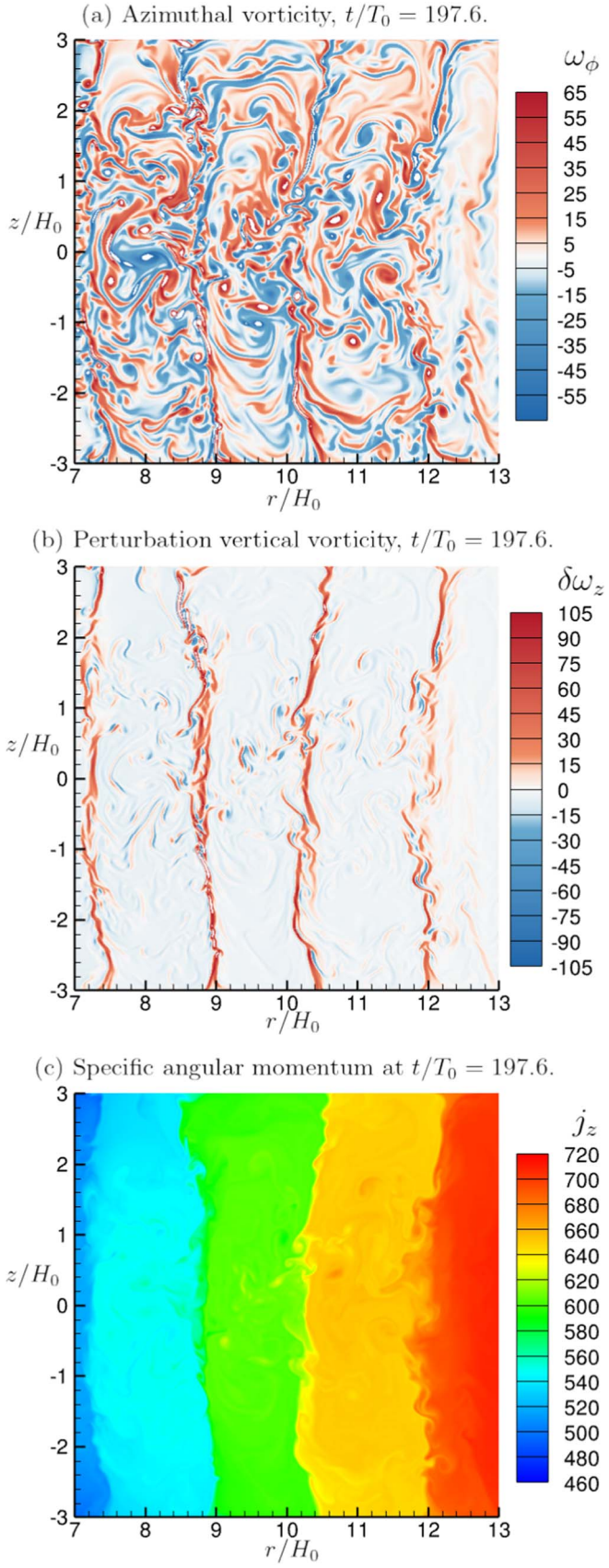

Figure 23. Axisymmetric simulation at $t/T_0 = 197.6$. This is a late time but is prior to the stationary state. In panel (a), the completely white regions have vorticity values beyond the range shown in the legend.

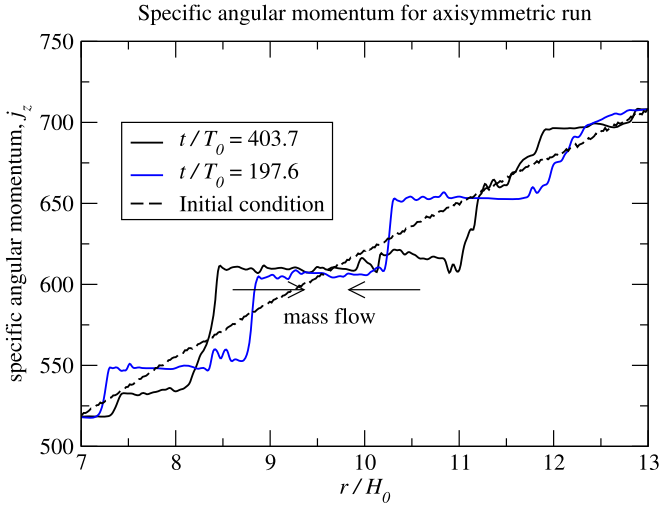

Figure 24. Axisymmetric run at late times. Specific angular momentum profile, $j_z = u_\phi r$, at the midplane.

One also observes that, compared to the 3D run (see Figure 2), the volume-averaged perturbation energy values are much larger, and the individual components are less isotropic. The vertical component, which is the strongest for $t/T_0 < 25$, now takes a back seat to the other two.

Figure 23 shows the perturbation azimuthal and vertical vorticity components at $t/T_0 = 197.6$, which is at a late time but prior to the stationary state. Their structure is very different from the 3D case and what is observed at early times in the axisymmetric case. The dominant component now is $\delta\omega_z$ rather than ω_ϕ, which translates to a larger magnitude of the azimuthal velocity perturbation compared to the vertical velocity. The shear layers of ω_ϕ that formed the edges of vertical jets at earlier times are still present, as is the pattern $\omega_\phi \lessgtr 0$ for $z \gtrless 0$ within these shear layers. However, the flow between the shear layers consists of large eddies and is reminiscent of 2D turbulence. Panel (b) shows that the ≈seven layers of vertical vorticity seen at $t/T_0 = 36.1$ (Figure 5) have now intensified, and only four remain. At a later time ($t/T_0 = 403.7$, not shown) only two such layers remain. In other words, flow length scales increase with time. The layers of strong $\delta\omega_z$ are associated with jumps in the total specific angular momentum $j_z = u_\phi r$ (panel (c)), which has a strong vertically coherent staircase profile with respect to r.

This can be seen more clearly in Figure 24, which shows the midplane profiles of $j_z(r)$ at $t/T_0 = 197.6$ and $t/T_0 = 403.7$. The latter is in the stationary state and has only two jumps in j_z. As shown earlier (Figure 4, blue line), in 3D there is no large-scale rearrangement of angular momentum, rather only a weak one in the upper layers of the disk. The circulation, $\Gamma_z = 2\pi j_z$, of circular material lines is proportional to j_z. Hence, by Stokes' theorem, a region of nearly constant $\Gamma_z(r)$ must be irrotational. For inviscid barotropic flow, Kelvin's theorem asserts that $\Gamma_z/Dt = 0$ for each circular material line. Hence, there are three possible mechanisms for the formation of the staircase structure: vertical transport of $j_z(z)$ given its vertical gradient (this being the mechanism that operates at early times), radial mixing of $j_z(r)$ by eddies between the shear layers, or baroclinic torque. For a circular material line, we have that

$$\frac{D\Gamma_z}{Dt} = \int_A \frac{1}{\rho^2}(\nabla\rho \times \nabla p) \cdot \hat{z}\, dS, \tag{55}$$

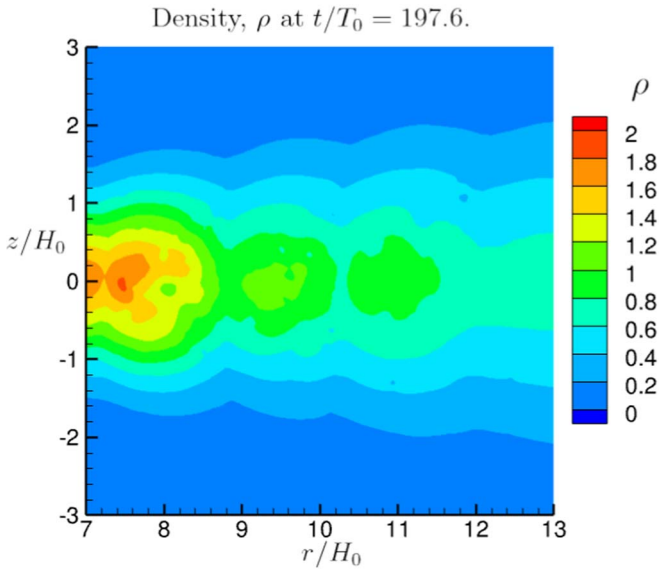

Figure 25. Density field for the axisymmetric simulation at $t/T_0 = 197.6$.

where A is the circular surface enclosed by the circle and $\hat{z}$ is the unit vector normal to the surface. However, the z-component of the baroclinic term in the integrand is zero for axisymmetric flow. The vertical gradient of j_z is weaker than its radial gradient, and radial velocity fluctuations are larger than vertical ones at late times. Hence, we conclude that radial mixing of j_z by eddies in regions bounded by vertical shear layers is responsible for the staircase profile of j_z at late times.

Accretion disk theory tells us that when angular momentum is redistributed, so is mass. Specifically, a fluid element that has a super-Keplerian j_z will move radially outward, and the opposite for sub-Keplerian j_z. A $j_z(r)$ profile that has flattened from a radially increasing Keplerian profile will cause mass to accumulate.

Figure 25 shows that mass becomes concentrated in the uniform-j_z regions observed in Figure 24.

In the axisymmetric simulations of MF24a there is also a clear difference between early and late times. Let us focus on their `dg3c4_2048` simulation. Their Figures 1 (left-hand plots) and 2 (top) show very many small steps in the j_z staircase at an earlier time. On the other hand, their Figure 11 shows the same run at 1360 orbits. Clearly, an increase of length scales has taken place, leading to only three jumps in j_z.

6. Present Lack of Large Persistent Vortices in the Interior of the Domain

Previous VSI simulations (N. Manger & H. Klahr 2018; M. Flock et al. 2020; M20; T. Pfeil & H. Klahr 2021) have reported the existence of one or more large persistent vortices (LPVs) and attributed their formation to a secondary RWI. We do not observe such vortices in the region not influenced by radial boundary conditions. The purpose of this section is to discuss this inconsistency in more detail.

6.1. Caveats for Applying RWI to VSI Simulations

RWI was first studied by R. V. E. Lovelace et al. (1999) assuming a *razor-thin* disk and conservation of the entropy,

$$S = P/\Sigma^\gamma, \tag{56}$$

following fluid particles. Here, P is the vertically integrated pressure, Σ is the surface density, and γ is the adiabatic exponent. A necessary condition for RWI is that, in the basic state, the function

$$\mathcal{L}(r) = \frac{\Sigma(r)}{2\omega_z(r)}[S(r)]^{2/\gamma} \tag{57}$$

has a local maximum. The thin-disk assumption is valid only for motions whose horizontal length scale $\ell \gg H(r)$. On the other hand, the radial size of LPVs observed in simulations is about $H(r)$. In addition, the locally isothermal equation of state, $p = \rho c_i^2(r)$, assumed in the present and other VSI simulations implies that radial motions *fail to conserve* S following fluid particles. Likewise, it remains to be shown whether *radiative* hydrodynamic VSI simulations that invoke RWI (e.g., M. Flock et al. 2020) possess an effective adiabatic exponent. Despite the lack of adiabaticity, previous works plot a vertically averaged $\mathcal{L}(r)$, presumably setting $\gamma = 1.4$. In spite of these caveats, it appears that the presence of LPVs in VSI simulations is correlated with some (but not all) local maxima in $\mathcal{L}(r)$, and we will discuss these simulations in the next subsection.

In previous VSI simulations, a diagnostic version of $\mathcal{L}(r)$ is defined using averages. For our case of a locally isothermal equation of state, $p = \rho c_i^2(r)$, we define the diagnostic

$$\mathcal{L}_{\rm diag}(r) = \frac{\langle\Sigma\rangle_{\phi t}}{2\langle\omega_z\rangle_{\phi z t}}\left[\frac{\langle\Sigma\rangle_{\phi t}\, c_i^2(r)}{\langle\Sigma\rangle_{\phi t}^{\gamma}}\right]^{2/\gamma}, \tag{58}$$

with $\gamma = 1.4$ and where, for example, $\langle . \rangle_{\phi z t}$ denotes an average with respect to ϕ, z, and t.

6.2. Previous VSI Simulations that Produced LPVs

The simulations of M. Flock et al. (2020) employed radiative hydrodynamics and produced a peak in $\alpha(r)$ (their Figure 2) in a region adjacent to the inner radial boundary. They explain the peak as being due to a radial decrease in thermal relaxation time (their Figure 13) to values that make VSI viable. The peak in $\alpha(r)$ led to a local dip in $\Sigma(r)$ (their Figure 1) and a pronounced maximum in the vertical vortensity $\omega_z(r, z = 0)/\Sigma$ (their Figure 5). These features in turn led to pronounced extrema in the RWI indicator function $\mathcal{L}(r)$ (their Figure B1), which is associated with one LPV. No *other* LPVs are generated in the rest of the domain. In summary, the trigger for an LPV in M. Flock et al. (2020) is a local $\alpha(r)$ peak induced by a favorable gradient in radiative relaxation time rather than by VSI dynamics.

More relevant is the work of M20, who for the same disk parameters as us observed the formation of multiple LPVs far from radial boundaries; see the lower-right panels in their Figures 8 and 10. Their t–R vortex trajectory plot (their Figure 12, lower-right panel) shows that the vortices have lifetimes of hundreds of orbits. Their Figure B1 (right-hand column) shows that the radial locations of these vortices are close to some, but not all, of the many maxima of their $\mathcal{L}$ diagnostic.

6.3. Present Simulations

Figure 26 plots $\omega_z/\Omega_{\rm K}(r)$ in the midplane for our main run; this is the same quantity plotted by M20. Note that their color map is such that values of $\omega_z/\Omega_{\rm K}(r) > 0.5$ have the same color

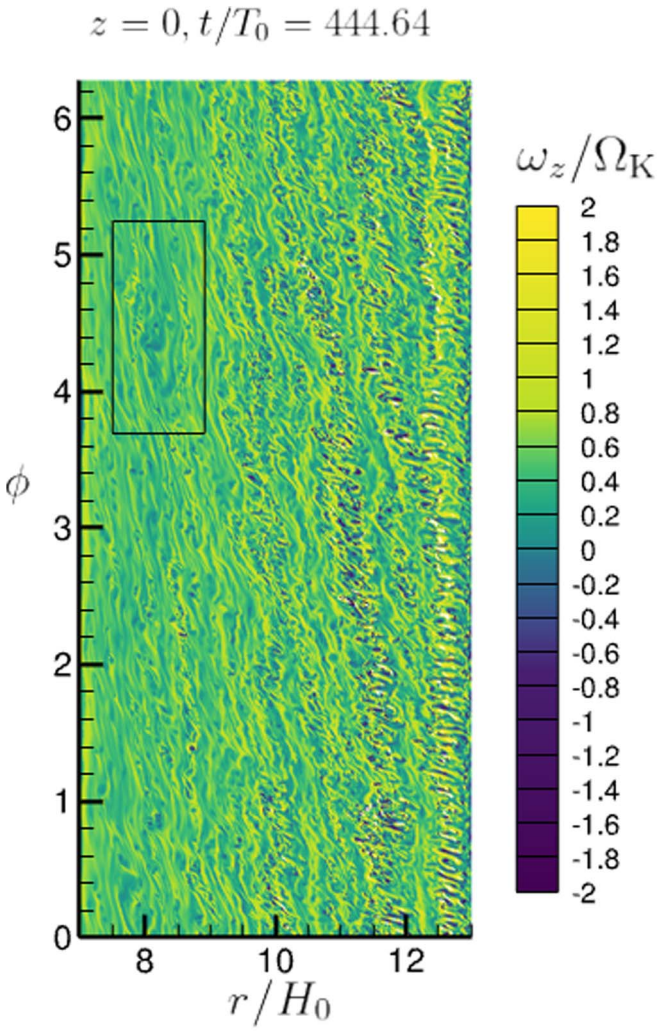

Figure 26. $\omega_z/\Omega_{\rm K}(r)$ in the midplane for the highest-resolution run.

(yellow) as $\omega_z/\Omega_{\rm K}(r) = 0.5$, and values of $\omega_z/\Omega_{\rm K}(r) < 0$ have the same color (dark blue) as $\omega_z/\Omega_{\rm K}(r) = 0$. As a result, their vortices appear darker than in our rendering. The background Keplerian value is $\omega_z/\Omega_{\rm K}(r) = 0.5$ and is rendered light green in Figure 26. The only large-scale coherent structure present is indicated by the box; it consists of several little whirls and filaments. It is centered at $r/H_0 \approx 8.2$, which is close to a local minimum in $\alpha(r)$; see black curve in Figure 19. This minimum is a result of proximity to the left radial boundary. A similar structure is present at this radial location as early as $t/T_0 = 69.5$.

Figure 27 plots the RWI diagnostic $\mathcal{L}_{\rm diag}(r)$ (black line) normalized by its value at r_0: It has a local maximum at $r/R_0 = 8.03$, which is close to the radial location of the vortex structure. The red line in Figure 27 shows that the surface density is a local minimum at this location. Another local maximum in $\mathcal{L}_{\rm diag}(r)$ is present at $r/H_0 \approx 12$ but is not associated with a large vortex.

Besides RWI, another mechanism known to produce LPVs is the SBI. The first requirement for instability is that the radial Brunt–Väisälä frequency squared,

$$N_r^2 = -\frac{1}{\gamma\rho}\frac{\partial p}{\partial r}\frac{\partial}{\partial r}\ln\left(\frac{p}{\rho^{\gamma}}\right), \tag{59}$$

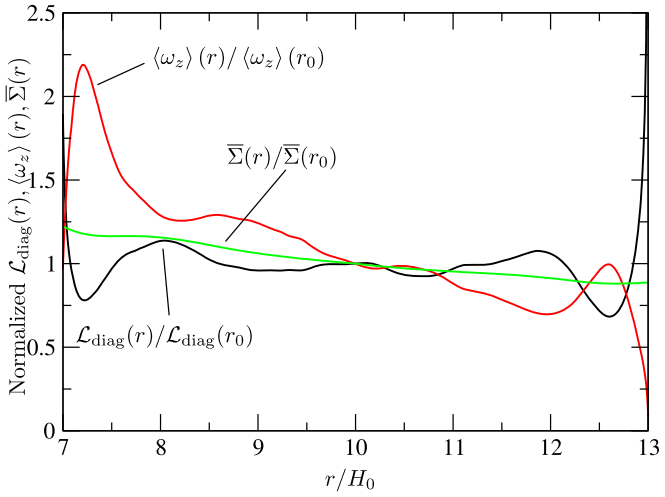

Figure 27. Black line: the diagnostic $\mathcal{L}_{\rm diag}(r)$ for the RWI. Red line: vertical vorticity ω_z averaged with respect to t, ϕ, and z. Green line: surface density Σ averaged with respect to t and ϕ. (Main run with a resolution of $512^2 \times 1024$.)

be negative. For the present basic state (Section 2.1), we have at the midplane that

$$N_r^2 = \frac{c_0^2}{\gamma r_0^2}(p+q)[p(\gamma-1)-q](r/r_0)^{q-2}. \tag{60}$$

For our case of $p=-3/2$ and $q=-1$, the coefficient in Equation (60) involving p and q equals -1; the first requirement is therefore satisfied. However, SBI also requires intermediate cooling times, $t_{\rm rad}$ (G. Lesur & J. C. B. Papaloizou 2010; P. Barge et al. 2016), whereas we have assumed that $t_{\rm rad}=0$.

6.4. Speculation

Why do M20 observe LPVs in the interior of the domain for the same disk parameters but we do not? The answer may lie in the link, discussed by MF24b, between maxima in $\mathcal{L}(r)$ and the $j_z(r)$ staircase that is prominent in axisymmetric $j_z(r)$. Specifically, a region of flattened $j_z(r)=u_\phi r$ corresponds to more irrotational flow ($u_\phi \approx {\rm const}/r$) and therefore suppressed ω_z. Since mass also accumulates in these regions, a local maximum is created in the first factor ($\Sigma/2\omega_z$) of $\mathcal{L}$. Therefore, one possibility is that M20 has a stronger $j_z(r)$ staircase in 3D than the present simulation, which leads to several $\mathcal{L}(r)$ maxima in the interior of the domain. It is tempting to attribute this to M20's lower resolution; however, our low-resolution simulations also failed to produce LPVs away from boundaries. Further effort is required to ascertain the reasons for this difference between our and the M20 simulation.

7. Closing Remarks

This work studied the vortical structure, Reynolds stresses, and midplane spectra of 3D turbulence driven by VSI (in the locally isothermal limit) for disk parameters $h=0.1$, $p=-1.5$, and $q=-1$. The salient points are as follows:

1. *Radial wavelength.* In axisymmetric VSI, the radial wavelength at early times corresponds to the most amplified linear mode, but then inexorably increases in time. In 3D, the ratio
$$\frac{\ell_r(r)}{\lambda_{r,\max}(r)} = [\pi|q|(H_0/R_0)]^{-1}\frac{\ell_r(r)}{H(r)} \tag{61}$$
of the radial wavelength, $\ell_r(r)$, to the most linearly amplified wavelength ($\lambda_{r,\max}$) increases from 2.4 to 4.4 as r increases from $8.6H_0$ to $11.6H_0$.
2. *Layers of positive* $\delta\omega_z$. Axisymmetric VSI has coherent vertical layers of $\delta\omega_z>0$ that increase in strength with $|z|$ and are coincident with interfaces between the upward and downward jets (Figure 5). Their formation and the preference for $\delta\omega_z>0$ can be explained by the vertical transport of specific angular momentum $j_z \equiv u_\phi r$ by the vertical jets. This phenomenon is equivalent to the formation of a staircase profile of $j_z(r)$ first discovered by H. Klahr et al. (2023), MF24a, and MF24b in their axisymmetric simulations. We find that these layers are also present in 3D but with much weaker jumps in specific angular momentum compared to the axisymmetric case (Figure 4(b)). These layers become stronger and more azimuthally coherent with increasing $|z|$ and undergo KH-like instability (Figure 13(a)), likely modified by background shear and rotation. The resulting vortices are small and possess all three vorticity components.
3. *Lack of large persistent* ω_z *vortices*. Absent are the large persistent RWI-driven vortices in the interior of the domain obtained by M20 for the same disk parameters. Rather, we observe only one large coherent structure (containing finer-scale features) near the left boundary of the domain where $\alpha(r)$ has an anomalous minimum due to boundary effects; the RWI diagnostic $\mathcal{L}_{\rm diag}(r)$ has a local maximum at this location (Figure 27). Flat regions in a $j_z(r)$ staircase, which is prominent in axisymmetric VSI, have a suppressed ω_z and accumulate mass that leads to peaks in the RWI indicator $\mathcal{L}(r)$ (MF24b). One may speculate that, due to lower resolution, M20 obtain a more pronounced j_z staircase in 3D than we do. However, our lower-resolution simulations also fail to display large persistent vortices. Therefore, further effort is needed to sort out this issue.
4. *Azimuthal vorticity.* In the axisymmetric case at early times, there is the following sign preference in the jet shear layers: $\omega_\phi \lessgtr 0$ for $z \gtrless 0$. By examining the two terms in the transport equation for ω_ϕ, we conclude that the perturbation in the vertical shear term is the dominant contributor to the production of ω_ϕ. The sign preference noted above is also visually noticeable in 3D.
5. *Midplane vorticity.* In 3D, the midplane contains many sheared filamentary vortical layers as well as many compact (nonfilamentary) vortices of roughly elliptical shape, having $\delta\omega_z<0$ and comparable values of $\delta\omega_r$ and $\delta\omega_\phi$.
6. *Variation of* α *with* r. There is a *linear increase of* $\alpha(r)$ with radius with a slope (at the highest resolution) of about 14% the midradius value per scale height. This increase currently lacks an explanation; it may be related to the increase of radial spacing, $\ell_r(r)$, with r that is faster than $H(r)$ (see item 1, which itself requires an explanation).
7. *Variation of* α *with resolution*. As the resolution is increased from a low value, α at first increases but then

decreases. M20 (their Table A1) observe an increase in α as resolution in increased for the same disk parameters as in the present work. Our value of α for an intermediate-resolution case is close to the value obtained by M20 for their highest-resolution case. It would be desirable in the future to obtain an $\alpha(r)$ that is converged as the grid is refined.

8. *Meridional flow.* We confirm the finding of M. R. Stoll et al. (2017) that there is a mean meridional radial flow toward the star for $|z| < H_0$ and outward for $|z| > H_0$, and that this flow is created by gradients of Reynolds shear stresses.
9. *Radial spectrum.* The spectrum of specific kinetic energy (velocity squared) at the midplane with respect to the radial wavenumber (k_r) was found to have a power-law region with an exponent of -1.82, close to the value of -2 for shear layers (A. A. Townsend & G. Taylor 1951). The spectrum is strongly dominated by the vertical velocity component.
10. *Azimuthal spectrum.* The spectrum with respect to the azimuthal wavenumber has a $-5/3$ power-law range, but with a small depression due to radial velocity fluctuations. Unlike M20 (their Figure 6), we do not find a -5 range.
11. *Late-time artifacts in axisymmetric VSI.* As discussed above, some features of the 3D simulation can be understood by appealing to physics in the early stage of the axisymmetric simulation. However, at late times the axisymmetric simulations have artifacts that are not present in 3D. These include increasing flow length scales and a strong staircase pattern in the specific angular momentum $j_\phi = u_\phi r$ with an accompanying redistribution of mass.

Acknowledgments

We are grateful to Dr. J. David Melon Fuksman (Max Planck Institut für Astronomie, Heidelberg) for his detailed comments, to Drs. Paul Estrada and Ted Manning at NASA Ames for performing a careful internal review, and to the referee for many useful suggestions that led to an improved manuscript. OMU acknowledges partial support from NASA's Theoretical and Computational Astrophysical Networks (TCAN) grant #80NSSC21K0497.

Appendix A
Padé Filter

This appendix briefly describes the fourth-order Padé filter (S. K. Lele 1992) which is applied after every time step as an implicit subgrid treatment. More details can be found in K. Shariff (2024). The attractiveness of Padé filters is their sharp cutoff. For a given unfiltered quantity u_i, its filtered outcome U_i on either a periodic domain or within the interior section of a nonperiodic domain is given by the solution of the following system of equations for every line of data in the mesh:

$$aU_{j-1} + U_j + aU_{j+1} = P(u_{j-2} + u_{j+2}) + Q(u_{j-1} + u_{j+1}) + Ru_j, \quad \text{(A1)}$$

for $j = 1, \ldots, n$, where n is the number of points along the line. For nonperiodic directions, the equations to be used at two points adjacent to each boundary are given in K. Shariff (2024). Equation (A1) constitutes a tridiagonal system that is solved along each data line in the mesh using the Thomas algorithm.

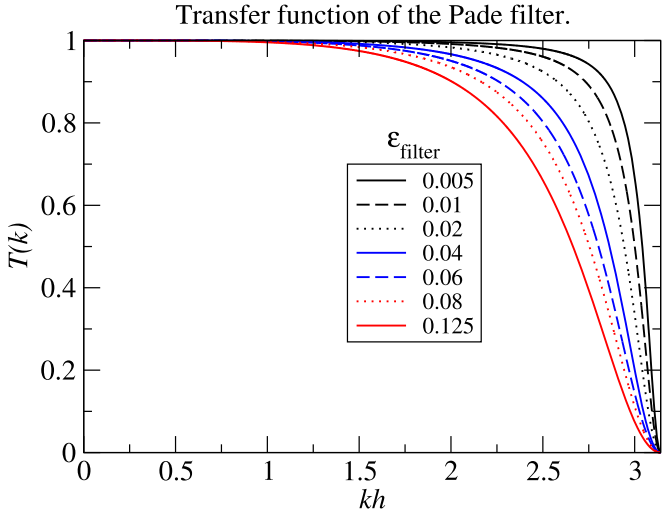

Figure 28. Transfer function for the Padé filter for various ϵ_{filter} covering the range used in the present simulations.

Regarding the coefficient Q in Equation (A1) as a free parameter, the condition that the leading-order difference between U_j and u_j be h^4, where h is the grid spacing, gives the rest of the coefficients as

$$a = -\frac{1}{2} + 2Q,$$
$$R = \frac{1}{2}(2 + 3a - 3Q),$$
$$P = \frac{1}{4}(a - Q). \quad \text{(A2)}$$

There is no filtering when $Q = 1/2$. To specify the strength of the filter, the code uses the parameter ϵ_{filter} such that

$$Q = \frac{1}{2} - \frac{1}{4}\epsilon_{\text{filter}}. \quad \text{(A3)}$$

The transfer function $T(k)$ of the filter versus wavenumber can be obtained by substituting $u_j = e^{ikx_j}$ and $U_j = T(k)e^{ikx_j}$ (with $x_j = jh$) into Equation (A1). Figure 28 shows $T(k)$ for values of ϵ_{filter} that cover the range $\epsilon_{\text{filter}} \in [0.015, 0.125]$ used in the present simulations.

Appendix B
Vorticity Equation for Axisymmetric VSI

For conservative body forces, the vorticity equation is given by

$$\frac{\partial \boldsymbol{\omega}}{\partial t} + \boldsymbol{u} \cdot \nabla\boldsymbol{\omega} = -\boldsymbol{\omega}\nabla \cdot \boldsymbol{u} + \boldsymbol{\omega} \cdot \nabla\boldsymbol{u} + \frac{\nabla\rho \times \nabla p}{\rho^2}. \quad \text{(B1)}$$

The terms on the rhs of Equation (B1) represent the change of vorticity by volumetric compression or expansion, tilting and stretching, and baroclinic torque. The compression/expansion term can be eliminated by introducing $\boldsymbol{\zeta} \equiv \boldsymbol{\omega}/\rho$.

Equation (B1) then becomes

$$\frac{\partial \boldsymbol{\zeta}}{\partial t} + \boldsymbol{u} \cdot \nabla \boldsymbol{\zeta} = \boldsymbol{\zeta} \cdot \nabla \boldsymbol{u} + \frac{\nabla \rho \times \nabla p}{\rho^3}. \tag{B2}$$

Using the expressions for $\boldsymbol{n} \cdot \nabla \boldsymbol{F}$ in cylindrical coordinates given in G. Batchelor (1967, Appendix 2), we have

$$\boldsymbol{u} \cdot \nabla \boldsymbol{\zeta} = (\boldsymbol{u} \cdot \nabla \zeta_z)\boldsymbol{e}_z + \left(\boldsymbol{u} \cdot \nabla \zeta_r + \frac{u_\phi \zeta_\phi}{r}\right)\boldsymbol{e}_r + \left(\boldsymbol{u} \cdot \nabla \zeta_\phi + \frac{u_\phi \zeta_r}{r}\right)\boldsymbol{e}_\phi \tag{B3}$$

and

$$\boldsymbol{\zeta} \cdot \nabla \boldsymbol{u} = (\boldsymbol{\zeta} \cdot \nabla u_z)\boldsymbol{e}_z + \left(\boldsymbol{\zeta} \cdot \nabla u_r - \frac{\zeta_\phi u_\phi}{r}\right)\boldsymbol{e}_r + \left(\boldsymbol{\zeta} \cdot \nabla u_\phi + \frac{\zeta_\phi u_r}{r}\right)\boldsymbol{e}_\phi. \tag{B4}$$

For $p = \rho c_{\rm i}^2(r)$, the baroclinic term becomes

$$\frac{\nabla \rho \times \nabla p}{\rho^3} = \frac{1}{\rho^2}\frac{\partial \rho}{\partial z}\frac{\partial c_{\rm i}^2}{\partial r}\boldsymbol{e}_\phi. \tag{B5}$$

Note that the baroclinic term acts only in the azimuthal direction. Let us begin by working on the ϕ vorticity equation. Using the fact that

$$\zeta_r = -\frac{1}{\rho}\frac{\partial u_\phi}{\partial z} \text{ and } \zeta_z = \frac{1}{\rho r}\frac{\partial}{\partial r}(r u_\phi), \tag{B6}$$

we get that

$$\boldsymbol{\zeta} \cdot \nabla u_\phi = \zeta_z \frac{\partial u_\phi}{\partial z} + \zeta_r \frac{\partial u_\phi}{\partial r} = \frac{1}{2\rho r}\frac{\partial u_\phi^2}{\partial z}. \tag{B7}$$

This term, which survives below, represents the tilting of ζ_r and ζ_z into ζ_ϕ. Since ζ_z includes the strong Keplerian vorticity, this is an important effect. So far, therefore, the ϕ vorticity equation becomes

$$\frac{D\zeta_\phi}{Dt} + \frac{u_\phi \zeta_r}{r} = \frac{\zeta_\phi u_r}{r} + \frac{1}{2\rho r}\frac{\partial u_\phi^2}{\partial z} + \frac{1}{\rho^2}\frac{\partial \rho}{\partial z}\frac{\partial c_{\rm i}^2}{\partial r}. \tag{B8}$$

This can be simplified further by noting that

$$\frac{D}{Dt}\left(\frac{\zeta_\phi}{r}\right) = \frac{1}{r}\frac{D\zeta_\phi}{Dt} - \frac{\zeta_\phi u_r}{r^2}. \tag{B9}$$

This gives

$$r\frac{D}{Dt}\left(\frac{\zeta_\phi}{r}\right) + \frac{u_\phi \zeta_r}{r} = \frac{1}{2\rho r}\frac{\partial u_\phi^2}{\partial z} + \frac{1}{\rho^2}\frac{\partial \rho}{\partial z}\frac{\partial c_{\rm i}^2}{\partial r}. \tag{B10}$$

Finally, introducing the expression in Equation (B6) for ζ_r into this gives the ϕ vorticity equation:

$$\boxed{\frac{D}{Dt}\left(\frac{\omega_\phi}{\rho r}\right) = \frac{1}{\rho r^2}\frac{\partial u_\phi^2}{\partial z} + \frac{1}{\rho^2 r}\frac{\partial c_{\rm i}^2}{\partial r}\frac{\partial \rho}{\partial z}.} \tag{B11}$$

Note that if the flow is nearly incompressible, i.e., $D\rho/Dt \approx 0$, then ρ can be removed from under the D/Dt. The hint for writing Equation (B11) in this form is an exercise in G. Batchelor (1967). The presence of r in the quantity being transported simply reflects the fact that, for axisymmetric flow, the stretching of ω_ϕ is purely geometric, i.e., as a circular vortex line increases in radius by a certain ratio, its ω_ϕ would increase by the same ratio if the rhs of Equation (B11) were zero. Equation (B11) implies that the creation of azimuthal vorticity, which takes the form of vertical jets in VSI, is influenced by both vertical shear and baroclinic torque. In the basic state, the two terms on the rhs of Equation (B11) oppose each other to give a zero left-hand side, and the signs of the two terms above and below the midplane are

$$0 = \frac{---}{+++} + \frac{+++}{---}, \tag{B12}$$

where a horizontal line represents the midplane. The z and r vorticity equations are

$$\frac{D\omega_z}{Dt} = \omega_r \frac{\partial u_z}{\partial r} + \omega_z \frac{\partial u_z}{\partial z} - \omega_z \nabla \cdot \boldsymbol{u}, \tag{B13}$$

$$\frac{D\omega_r}{Dt} = \omega_z \frac{\partial u_r}{\partial z} + \omega_r \frac{\partial u_r}{\partial r} - \omega_r \nabla \cdot \boldsymbol{u}. \tag{B14}$$

The three terms on each rhs represent tilting, stretching, and volumetric compression, respectively. Note again that the baroclinic term enters only the ω_ϕ equation.

Appendix C
Reynolds-averaged Conservation Equations Using the Favre Decomposition

The purpose of Appendices C and D is to rigorously derive the residual stress that arises when the governing equations are Reynolds averaged. The presentation is necessary given the different expressions used in the simulation literature.

In the absence of magnetic torques and when the gravitational potential (Φ) is axisymmetric, the inviscid equations for conservation of mass and momentum equations read

$$\frac{\partial \rho}{\partial t} + \nabla \cdot (\rho \boldsymbol{u}) = 0, \tag{C1}$$

$$\frac{\partial}{\partial t}(\rho u_\phi r) + \nabla \cdot (\rho u_\phi r \boldsymbol{u}) = -\frac{\partial p}{\partial \phi}, \tag{C2}$$

$$\frac{\partial}{\partial t}(\rho u_r) + \nabla \cdot (\rho u_r \boldsymbol{u}) - \rho\frac{u_\phi^2}{r} = -\frac{\partial p}{\partial r} - \rho\frac{\partial \Phi}{\partial r}, \tag{C3}$$

$$\frac{\partial}{\partial t}(\rho u_z) + \nabla \cdot (\rho u_z \boldsymbol{u}) = -\frac{\partial p}{\partial z} - \rho\frac{\partial \Phi}{\partial z}, \tag{C4}$$

where the divergence operator is

$$\nabla \cdot \boldsymbol{F} \equiv \frac{\partial F_z}{\partial z} + \frac{1}{r}\frac{\partial}{\partial r}(r F_r) + \frac{1}{r}\frac{\partial F_\phi}{\partial \phi} = 0. \tag{C5}$$

We take the average of these equations with respect to azimuth and time over a period $[t_1, t_2]$ long enough to ensure converged statistics and during which the flow has attained statistical stationarity in time. The averaging operator, denoted by a bar, is therefore

$$\overline{f}(r, z) = \frac{1}{2\pi(t_2 - t_1)}\int_0^{2\pi} d\phi \int_{t_1}^{t_2} dt f(r, z, \phi, t). \tag{C6}$$

This average satisfies all the axioms required for being a *Reynolds* average. Throughout, one can omit the time average if desired; the only change this results in is the appearance of $\partial/\partial t$ of mean quantities in Equations (C15)–(C18).

Consider the Reynolds average, $\overline{\rho u v}$, of a generic triple product which appears in the momentum equations. If we

introduce the Reynolds decomposition $u = \bar{u} + u'$ and $v = \bar{v} + v'$, we get

$$\overline{\rho u v} = \bar{\rho}\,\bar{u}\,\bar{v} + \overline{\rho u' v'} + \bar{u}\,\overline{\rho v'} + \bar{v}\,\overline{\rho u'}. \tag{C7}$$

The last two terms make this unwieldy. Note that M. R. Stoll & W. Kley (2014, Equation (15)) and R. P. Nelson et al. (2013) ignore the last two terms in their computation of the $r\phi$ Reynolds stress and perform the averaging over the inhomogeneous radial direction.

To allow averages of triple products involving the density ρ to be written compactly, one introduces a density-weighted average, denoted by a tilde, which is known as a A. Favre (1969) average:

$$\widetilde{f} \equiv \frac{\overline{\rho f}}{\bar{\rho}}. \tag{C8}$$

Fluctuations with respect to the Favre average are denoted by double primes:

$$f = \widetilde{f} + f''. \tag{C9}$$

An important relation which we shall use below is that

$$\overline{\rho f''} = \overline{\rho(f - \widetilde{f})} = \overline{\rho f} - \overline{\rho \widetilde{f}} = \overline{\rho f} - \widetilde{f}\,\bar{\rho} \tag{C10}$$

$$= \overline{\rho f} - \frac{\overline{\rho f}}{\bar{\rho}}\bar{\rho} = 0, \tag{C11}$$

since $\widetilde{f}$ is already an average. Specifically, Equation (C11) allows one to write triple products as

$$\overline{\rho u v} = \overline{\rho\,\tilde{u}\,\tilde{v}} + \overline{\rho u'' v''} + \overline{\rho \tilde{u} v''} + \overline{\rho u'' \tilde{v}} \tag{C12}$$

$$= \bar{\rho}\,\tilde{u}\,\tilde{v} + \overline{\rho u'' v''} + \tilde{u}\,\overline{\rho v''} + \tilde{v}\,\overline{\rho u''} \tag{C13}$$

$$= \bar{\rho}\,\tilde{u}\,\tilde{v} + \overline{\rho u'' v''}, \tag{C14}$$

which is a little more compact than Equation (C7).

Decomposing flow variables as in Equation (C9), applying the bar average to the conservation Equations (C1)–(C4), using the above relations, assuming statistical stationarity and that the gravitational potential has no fluctuation, gives

$$\nabla_{rz} \cdot (\bar{\rho}\tilde{\boldsymbol{u}}) = 0, \tag{C15}$$

$$\nabla_{rz} \cdot (\bar{\rho}\tilde{u}_\phi r\tilde{\boldsymbol{u}} + \overline{\rho u_\phi'' r\boldsymbol{u}''}) = 0, \tag{C16}$$

$$\nabla_{rz} \cdot (\bar{\rho}\,\tilde{u}_r\,\tilde{\boldsymbol{u}} + \overline{\rho\,u_r''\,\boldsymbol{u}''}) - \bar{\rho}\frac{(\tilde{u}_\phi)^2}{r} - \frac{\overline{\rho u_\phi''^2}}{r}$$

$$= -\frac{\partial \bar{p}}{\partial r} - \bar{\rho}\frac{\partial \Phi}{\partial r}, \tag{C17}$$

$$\nabla_{rz} \cdot (\bar{\rho}\,\tilde{u}_z\tilde{\boldsymbol{u}} + \overline{\rho\,u_z''\,\boldsymbol{u}''}) = -\frac{\partial \bar{p}}{\partial z} - \bar{\rho}\frac{\partial \Phi}{\partial z}, \tag{C18}$$

where $\nabla_{rz}\cdot$ denotes the divergence operator equation (C5) restricted to the rz plane. The above equations contain the Reynolds stresses

$$T_{ab} = \overline{\rho\,u_a''\,u_b''}, \quad a, b \in \{z, r, \phi\}. \tag{C19}$$

Appendix D
Calculation of Reynolds Stresses

This appendix explains how to efficiently calculate Reynolds stresses with fluctuations defined with respect to the time-ϕ averaged flow. By efficiently, we mean without having to store entire flow fields in order to obtain the time mean. The Reynolds stress is defined as

$$T_{ab} \equiv \overline{\rho u_a'' u_b''}, \tag{D1}$$

where the bar denotes an average with respect to ϕ and t, while a and b represent the cylindrical coordinate indices r, z, or ϕ. A double prime denotes a Favre fluctuation, e.g.,

$$u_a'' = u_a - \tilde{u}_a, \tag{D2}$$

where the tilde signifies the Favre average:

$$\tilde{u}_a \equiv \overline{\rho u_a}/\bar{\rho}. \tag{D3}$$

As a simulation proceeds, one does not have the time average and therefore cannot calculate the temporal fluctuations needed to accumulate T_{ab}. However, the following simple algebra allows one to store only ϕ averages at sample times and calculate the time average as a post-processing step. Using Equation (D2), we have

$$T_{ab} \equiv \overline{\rho u_a'' u_b''} = \overline{\rho(u_a - \tilde{u}_a)(u_b - \tilde{u}_b)}. \tag{D4}$$

Expanding Equation (D4) gives

$$T_{ab} = \overline{\rho u_a u_b} + \overline{\rho \tilde{u}_a \tilde{u}_b} - \overline{\rho \tilde{u}_a u_b} - \overline{\rho u_a \tilde{u}_b}. \tag{D5}$$

Now, every Favre average such as $\tilde{u}_a$ is independent of ϕ and t and can be pulled out from under the bar operation, giving

$$T_{ab} = \overline{\rho u_a u_b} + \bar{\rho}\tilde{u}_a\tilde{u}_b - \tilde{u}_a\overline{\rho u_b} - \tilde{u}_b\overline{\rho u_a}. \tag{D6}$$

Next, using the definition of the Favre average gives

$$T_{ab} = \overline{\rho u_a u_b} + \bar{\rho}\frac{\overline{\rho u_a}}{\bar{\rho}}\frac{\overline{\rho u_b}}{\bar{\rho}} - \frac{\overline{\rho u_a}}{\bar{\rho}}\overline{\rho u_b} - \frac{\overline{\rho u_b}}{\bar{\rho}}\overline{\rho u_a}. \tag{D7}$$

Finally, the second and third terms cancel, giving the final expression:

$$T_{ab} = \overline{\rho u_a u_b} - \frac{1}{\bar{\rho}}\overline{\rho u_a}\,\overline{\rho u_b}. \tag{D8}$$

To compute Equation (D8) we store ϕ averages of $\rho u_a u_b$, ρu_a, and ρ at a sample of times during the simulation, during the period when statistical stationarity has been achieved. Then, as a post-processing step, a further time average is computed to complete the bar operation. Finally, the Reynolds stresses are obtained using Equation (D8). Equation (D8) can also be used when the time average is skipped and only a ϕ average is included.

ORCID iDs

Karim Shariff https://orcid.org/0000-0002-7256-2497
Orkan M. Umurhan https://orcid.org/0000-0001-5372-4254

References

Arlt, R., & Urpin, V. 2004, A&A, 426, 755
Barge, P., Richard, S., & Le Dizès, S. 2016, A&A, 592, A136
Barker, A. J., & Latter, H. N. 2015, MNRAS, 450, 21
Batchelor, G. 1967, An Introduction to Fluid Dynamics (Cambridge: Cambridge Univ. Press)
Boris, J. P., Grinstein, F. F., Oran, E. S., & Kolbe, R. L. 1992, FlDyR, 10, 199
Craik, A. D. D., Criminale, W. O., & Gaster, M. 1986, RSPSA, 406, 13
Cui, C., & Latter, H. N. 2022, MNRAS, 512, 1639
Dutton, J. 1963, JAtS, 20, 107
Estrada, P., & Umurhan, O. 2023, ApJ, 946, 15
Falkovich, G., & Lebedev, V. 2011, PhRvE, 83, 045301
Favre, A. 1969, Problems of Hydrodynamics and Continuum Mechanics, Contributions in Honor of the 60th Birthday of L.I. Sedov, 14th Nov. 1967 (Philadelphia, PA: Soc. for Industrial and Applied Mathematics), 231

Flock, M., Fromang, S., Turner, N. J., & Benisty, M. 2017, ApJ, 835, 230
Flock, M., Turner, N., Nelson, R., et al. 2020, ApJ, 897, 155
Flores-Rivera, L., Flock, M., & Nakatani, R. 2020, A&A, 644, A50
Fricke, K. 1968, ZAp, 68, 317
Fukuhara, Y., Okuzumi, S., & Ono, T. 2021, ApJ, 914, 132
Goldreich, P., & Schubert, G. 1967, ApJ, 150, 571
Jiménez, J. 1996, JFM, 313, 223
Kida, S. 1981, JPSJ, 50, 3517
Klahr, H., Baehr, H., & Fuksman, J. M. 2023, arXiv:2305.08165
Klahr, H. H., & Bodenheimer, P. 2003, ApJ, 582, 869
Latter, H. N., & Papaloizou, J. 2018, MNRAS, 474, 3110
Lele, S. K. 1992, JCoPh, 103, 16
Lesur, G., Flock, M., Ercolano, B., et al. 2022, in ASP Conf. Ser.. 534, Protostars and Planets VII, ed. S. Inutsuka et al. (San Francisco, CA: ASP), 465
Lesur, G., & Papaloizou, J. C. B. 2010, A&A, 513, A60
Lin, M.-K., & Youdin, A. 2015, ApJ, 811, 17
Lovelace, R. V. E., Li, H., Colgate, S. A., & Nelson, A. F. 1999, ApJ, 513, 805
Manger, N., & Klahr, H. 2018, MNRAS, 480, 2125
Manger, N., Klahr, H., Kley, W., & Flock, M. 2020, MNRAS, 499, 1841
Melon Fuksman, J. D., Flock, M., & Klahr, H. 2024a, A&A, 682, A140
Melon Fuksman, J. D., Flock, M., & Klahr, H. 2024b, A&A, 682, A139
Nelson, R. P., Gressel, O., & Umurhan, O. M. 2013, MNRAS, 435, 2610
Pfeil, T., & Klahr, H. 2021, ApJ, 915, 130
Richard, S., Nelson, R. P., & Umurhan, O. M. 2016, MNRAS, 456, 3571
Ritos, K., Kokkinakis, I., & Drikakis, D. 2018, CF, 173, 307
Schäfer, U., Johansen, A., & Banerjee, R. 2020, A&A, 635, A190
Shakura, N. I., & Sunyaev, R. A. 1973, A&A, 24, 337
Shariff, K. 2024, ApJS, 273, 37
Smagorinsky, J. 1963, MWRv, 91, 99
Stoll, M. R., & Kley, W. 2014, A&A, 572, A77
Stoll, M. R., & Kley, W. 2016, A&A, 594, A57
Stoll, M. R., Kley, W., & Picogna, G. 2017, A&A, 599, L6
Townsend, A. A., & Taylor, G. 1951, RSPSA, 208, 534
Umurhan, O. M., Nelson, R. P., & Gressel, O. 2016, A&A, 586, A33
Urpin, V. 2003, A&A, 404, 397
Urpin, V., & Brandenburg, A. 1998, MNRAS, 294, 399